

Architecture in Stiff Biological Materials: a Template for Toughness Enhancement, or a Siren Song?

Michael A. Monn¹, Kaushik Vijaykumar¹, Sayaka Kochiyama¹, and Haneesh Kesari*¹

¹*School of Engineering, Brown University, Providence, RI, USA*

Keywords: structure-property relationships, *Euplectella aspergillum*, fracture toughness, R-curves, biological composites

Some stiff biological materials, such as shells and bones, have surprisingly high fracture toughness compared to their brittle ceramic constituents. These materials are heterogeneous and consist of layers of ceramic phases separated by thin organic interlayers. Understanding the link between layered architectures and toughness could help to identify new ways to improve the toughness of engineering composites. We study one instance of the layered architecture found in the skeletal elements—called spicules—of the marine sponge *Euplectella aspergillum*. The spicules contain cylindrical layers composed of silica. We cut micrometer-size notches in the spicules and perform flexural tests on them to measure their fracture initiation toughness and average crack growth resistance. We found that the spicule’s architecture provides up to a ten-fold enhancement to its fracture initiation toughness. We also found that it provides approximately a two-fold enhancement to its average crack growth resistance. However, compared to some other prototypically tough biological materials, like nacre, the toughness enhancements provided by the spicule’s architecture are relatively small. We investigate the reasons underlying the lack of toughness enhancement using computational fracture mechanics simulations. The combination of mechanical characterization and computational mechanics simulations presented here provides a framework for developing a more complete understanding of how toughness enhancing mechanisms can be induced or suppressed by changing the geometry of a layered architecture.

¹ Despite being primarily composed of brittle ceramics, some stiff biological materials (SBMs), such as bones and shells, are remarkably tough .^[?, ?, ?, ?] For example, nacre—the iridescent material found in mollusk shells—is composed of >95% aragonite (a brittle, calcium carbonate mineral) by volume yet it has a specific fracture initiation toughness on par with nylon and some iron alloys .^[?] A material’s fracture toughness quantifies its ability to prevent the growth of pre-existing cracks or flaws, and therefore be resistant to catastrophic failure. These tough SBMs are often heterogeneous and are composed of alternating layers of ceramic and organic materials (see **Figure 1**). The arrangements of these layers, which we refer to as layered architectures, are thought to be responsible for the toughness enhancements

9 observed in these SBMs .^[?] There is currently considerable interest in understanding the connections
 10 between layered architectures and toughness enhancements in SBMs ^[?, ?, ?, ?] because this understanding
 could aid in the development of new, tough engineering materials .^[?, ?, ?]

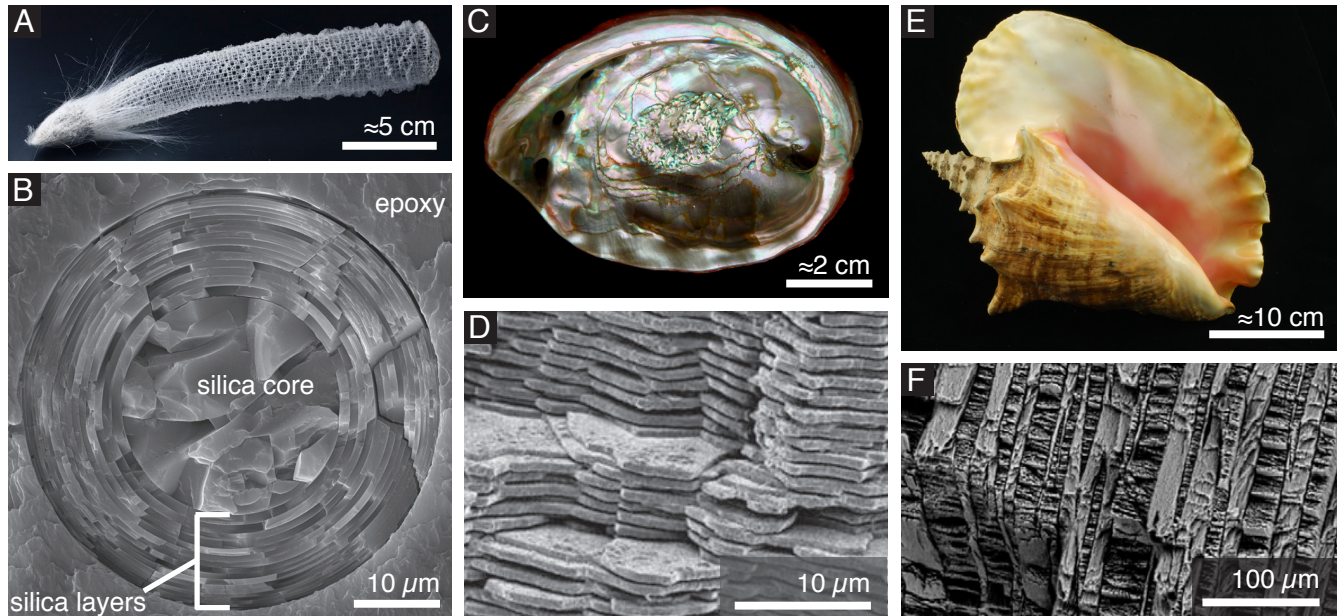


Figure 1. Examples of the layered architecture in SBMs. (A) Skeleton of a *Euplectella aspergillum* sponge (modified from ^[?] copyright 2015, The National Academy of Sciences). (B) Concentric silica layers make up the cylindrical layered architecture of anchor spicules from *E. aspergillum* (modified from ^[?] copyright 2015, The National Academy of Sciences). (C) The iridescent shell of *Haliotis rufescens* (courtesy of John Varner). (D) The brick and mortar layered architecture of nacre consisting of staggered aragonite tablets (modified with permission from ^[?] copyright 2012, the Royal Society of Chemistry). (E) The shell of the queen conch (*Strombus gigas*) (courtesy of John Varner). (F) The crossed-layered architecture of the *S. gigas* shell, which consists of layers of aragonite (modified with permission from ^[?] copyright 2014, Elsevier).

11
 12 A number of SBMs, including nacre and bone, have served as models for the seminal research on un-
 13 derstanding these connections .^[?, ?] Recently, the anchor spicules of the marine sponge *Euplectella*
 14 *aspergillum* (*Ea.*) have been added to this group of model SBMs .^[?, ?, ?, ?] The anchor spicules are hair-
 15 like fibers that attach *Ea.* to the soft sediment of the sea floor where it lives (see **Figure 2 (A)–(B)**)
 16 .^[?] Each of the thousands of anchor spicules in a *Ea.* sponge is approximately 10 cm long and 50 μm
 17 in diameter. Viewed in cross-section, an anchor spicule consists of a solid cylindrical core surrounded
 18 by \approx 25 concentric, cylindrical layers (see Figure 1 (B) and 2 (C)) .^[?, ?, ?] Both the core and the layers
 19 are composed of silica and adjacent silica layers are separated by a thin (\approx 5–10 nm ^[?]) organic inter-
 20 layer. Similar cylindrical layered architectures have also been found in spicules from a number of related
 21 sponge species .^[?, ?, ?, ?]

22 Many previous studies of *Ea.* anchor spicules suggest that like the layered architectures of nacre and

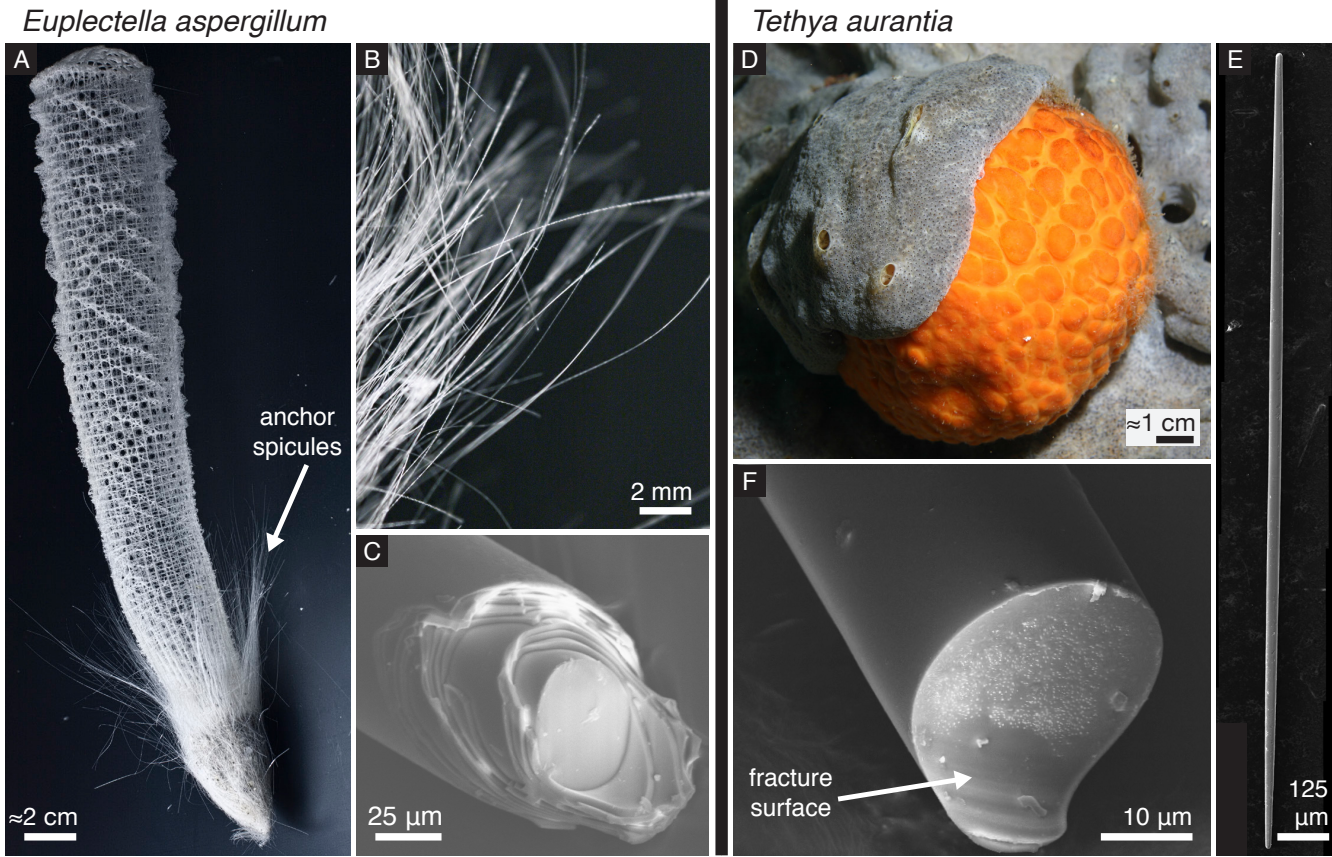


Figure 2. The skeletons and spicules of *Ea.* and *Ta.* sponges. (A) The skeleton of the *Ea.* sponge (modified from [?] copyright, the National Academy of Sciences). (B) The anchor spicules that fasten the sponge to the seafloor (modified from [?] copyright, the National Academy of Sciences). (C) The broken end of an *Ea.* anchor spicule that was fracture in three-point bending showing its layered architecture (modified from [?] copyright 2017, Elsevier). (D) A *Ta.* sponge (image courtesy of Steve Lonhart/NOAA MBNMS). (E) A toothpick-like spicule found within the *Ta.* sponge (reproduced from [?] under the Creative Commons 4.0 BY license). (F) The exposed surface of a *Ta.* spicule that was fractured in the same way as the *Ea.* spicule shown in (C) showing that it does not contain a layered architecture (modified from [?] copyright 2017, Elsevier).

other tough SBMs, the spicule's cylindrical layered architecture also enhances fracture toughness . [?, ?, ?, ?]
 None of these studies, however, provide direct measurements of the *Ea.* spicule's fracture toughness, nor by other means do they quantify how much the architecture enhances the spicule's toughness compared to that of its constituent silica. These measurements and comparison are critical for determining whether the *Ea.* spicules should be used as a template for bioinspired materials with enhanced toughness.
 We measured the *Ea.* spicule's fracture toughness by cutting micrometer-size notches in the spicules using a focused ion beam and performing flexural tests on them (see Section 2.1). The notches ranged in length from approximately 7% to 64% of the spicule's diameter. During the flexural test, a notched spicule was bent until a crack grew from the notch and fractured it (see Figure 3 (A)–(B)). We measured the force applied to a spicule during the test and the lateral deflection of its cross-section at the location

33 the load was applied. Using these data, we computed the spicule's fracture toughness (see Sections 2.3
34 and 2.4).

35 To quantify the toughness enhancement provided by the *Ea.* spicule's architecture, we compared its
36 fracture toughness to the fracture toughness of spicules from a related sponge, *Tethya aurantia* (*Ta.*) (see
37 Figure 2 (D)–(F)). The *Ta.* spicules have a similar chemical composition and bonding structure to the *Ea.*
38 spicules ,^[?] but do not possess a layered architecture (see Figure 2 (F)) .^[?] They are ≈2 mm long, ≈35
39 μm in diameter and have a needle-like shape. That is, they are thickest at the midpoint along their length
40 and taper to become thinner toward their ends (see Figure 2 (E)). We measured the *Ta.* spicules' fracture
41 toughness using the same type of notched flexural test that we performed on the *Ea.* spicules (see Section
42 2).

43 Overall, we found that the toughness enhancement provided by the *Ea.* spicule's architecture is much
44 smaller than that provided by architectures seen in prototypically tough SBMs, like nacre and bone (see
45 Section 2.5). While these tough SBMs also possess layered architectures, the layers in these materials are
46 flat rather than cylindrical/curved (see Figure 1). For very short notches (less than 10% of the spicule's
47 diameter), we observed that the *Ea.* spicule's architecture did provide up to a 10 fold increase in fracture
48 initiation toughness. However, this enhancement is still relatively small compared to that observed in
49 nacre. This observed increase in fracture initiation toughness is consistent with the crack tip shielding
50 effect described by .^[?] We discuss the increased initiation toughness enhancement for short notches in
51 greater detail in Section 2.3.

52 We investigated the difference in the toughness enhancements provided by the cylindrical and flat layered
53 architectures using computational mechanics simulations (see Section 3). In the simulations we used
54 a regularized variational fracture method ^[?] to predict how both cylindrical and flat layers affect crack
55 growth. We compared the mechanical response and crack pattern in a specimen containing two cylindrical
56 layers to a specimen containing two flat layers. We found that while crack arrest and re-nucleation
57 appears to be the dominant toughening mechanism in the flat layered architecture, it does not manifest
58 to the same extent in the cylindrical layered architecture. Thus, the curvature of the *Ea.* spicules' layers
59 could fundamentally change the toughening mechanisms operating within them compared to SBMs with
60 flat layered architectures.

61 1 Recapitulation of the concept of fracture toughness

62 Roughly speaking, fracture toughness—also known as crack growth resistance, R —is the amount of
 63 energy that a crack consumes to grow its area by a unit amount. If the energy consumed does not depend
 64 on the geometries of the crack, the crack increment, the specimen, and the specimen's architecture then
 65 R is considered to be a material property. However, in SBMs the value of R can depend on the length that
 66 the crack has grown, Δa (see **Figure 3 (B)–(C)**). The value of R when a crack first starts growing, $R(0)$, is
 67 known as the fracture initiation toughness. If the value of R increases with Δa , then the material is said to
 68 have a rising R curve (see e.g., Figure 3 (C)). In this case, as the crack grows the material becomes more
 69 resistant to crack growth. Several SBMs like nacre and bone [?, ?, ?, ?] as well as in synthetic materials with
 70 architectures inspired by these SBMs (see Figure 3 (C)) [?] display rising R curves. In these materials,
 71 the rise in R is caused by toughening mechanisms that become activated as a crack grows and interacts
 with the layered architecture.

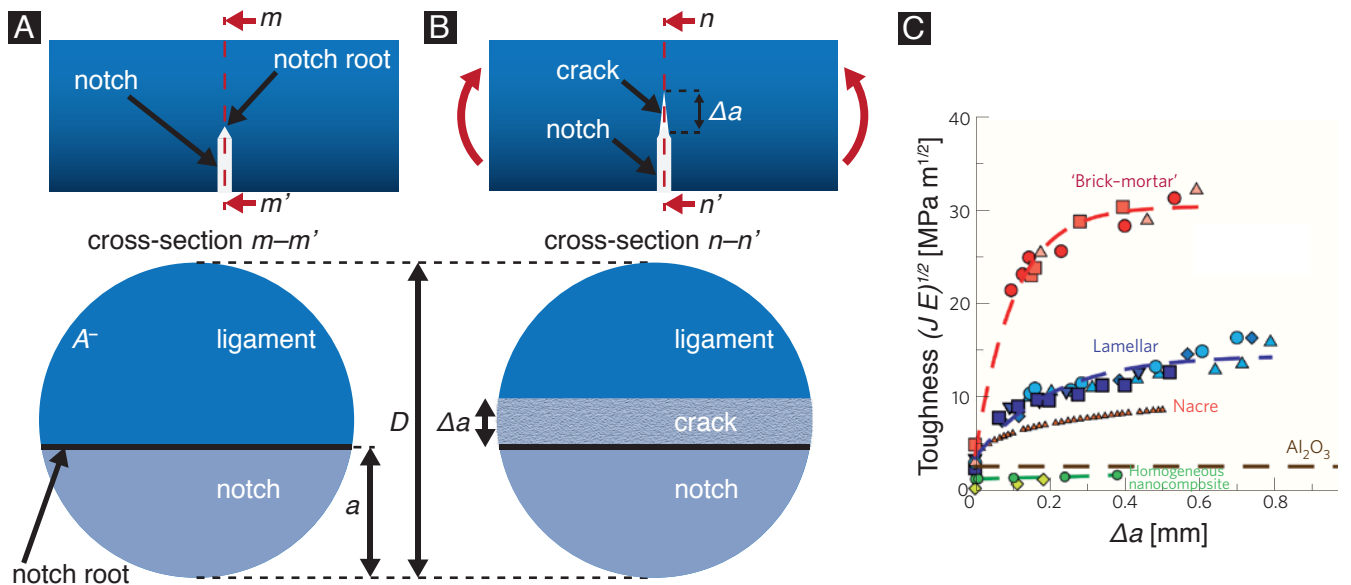


Figure 3. Fracture toughness. (A) Geometry of a fracture test specimen with a notch cut in it. A cross-sectional view shows the notch length, a , and ligament area, A^- . (B) When loaded in flexure, a crack grows from the notch root. The crack length, Δa is shown in the corresponding cross-sectional view. (C) Crack growth resistance curves of nacre, nacre-inspired composites made of aluminum oxide tablets, and monolithic aluminum oxide obtained by [?] and [?]. The crack growth resistance is given here in terms of the J -integral (modified with permission from [?] copyright Nature Publishing Group).

72

73 We measured $R(0)$ and $\langle R \rangle$ —i.e., the average value of R (see Section 2.4 for details)—for the *Ea.* anchor
 74 spicules and the *Ta.* spicules (see Section 2). By comparing $R(0)$ and $\langle R \rangle$ of the *Ea.* spicules to $R(0)$
 75 and $\langle R \rangle$ of the *Ta.* spicules, we quantified the toughness enhancement provided by the *Ea.* spicule's

Table 1. Summary of specimen geometry for *Ea.* and *Ta.* spicules^{a)}. Values for D , L and a listed as mean±standard error of measurement

Species	No. specimens	L [μm]	D [μm]	a [μm]
<i>E. aspergillum</i>	35	799.25±6.35	41.42±2.16	12.92±1.30
<i>T. aurantia</i>	26	725.86±18.36	32.28±1.07	6.96±0.80

^{a)} see Tables S1 and S2 for details of the geometry of individual *Ea.* and *Ta.* specimens.

76 architecture both at fracture initiation and during crack growth (see Section 2.5).

77 2 Results

78 To measure $R(0)$ and $\langle R \rangle$, we performed flexural tests on 35 *Ea.* and 26 *Ta.* spicules using a configuration
 79 similar to that described by Jaya et al .^[?, ?, ?] We placed a spicule across a trench that was cut in a steel
 80 plate and ensured that its longitudinal axis was perpendicular to the trench edges (see **Figure 4** (A)). We
 81 used trenches whose spans were nominally 600 to 800 μm and measured the span of each trench, L , from
 82 optical micrographs (see **Table 1** for a summary and **Tables S1** and **S2** for measurement details). We then
 83 glued the ends of the spicule to the steel plate so that only the section suspended over the trench remained
 84 exposed.

85 The spicule specimen's undeformed configuration can be described using the orthonormal set of Cartesian
 86 basis vectors $\{\hat{e}_1, \hat{e}_2, \hat{e}_3\}$ (**Figure 4** (A), (B), and (D)), which correspond to the Cartesian coordinates
 87 $\{x_1, x_2, x_3\}$. The origin of this coordinate system, denoted as \mathcal{O} , is located at the point on the spicule's
 88 central, longitudinal axis directly above the left trench edge (see **Figure 4** (A)).

89 We cut a notch through part of the spicule's cross-section located mid way across the trench (i.e., at
 90 $x_1 = L/2$) using a focused ion beam (FIB) (see **Figure 4** (A)–(B) and Section 5.2). A representative
 91 micrograph of a notched spicule is shown in **Figure 4** (C). **Figure 4** (D) depicts a schematic representation
 92 of the spicule's cross-section at $x_1 = L/2$ in which the notched region is shown in light blue and the
 93 remaining ligament is shown in dark blue. We refer to the apex or tip of the notch as the notch root. The
 94 notch root is a straight line segment that is parallel to \hat{e}_3 , see **Figure 4** (D)). After cutting the notch, we
 95 imaged the spicule using the FIB and measured the diameter of the spicule's cross-section at $x_1 = L/2$,

96 D , and the notch length, a , from the micrographs (see Table 1 for a summary and Tables S1 and S2 for
measurement details).

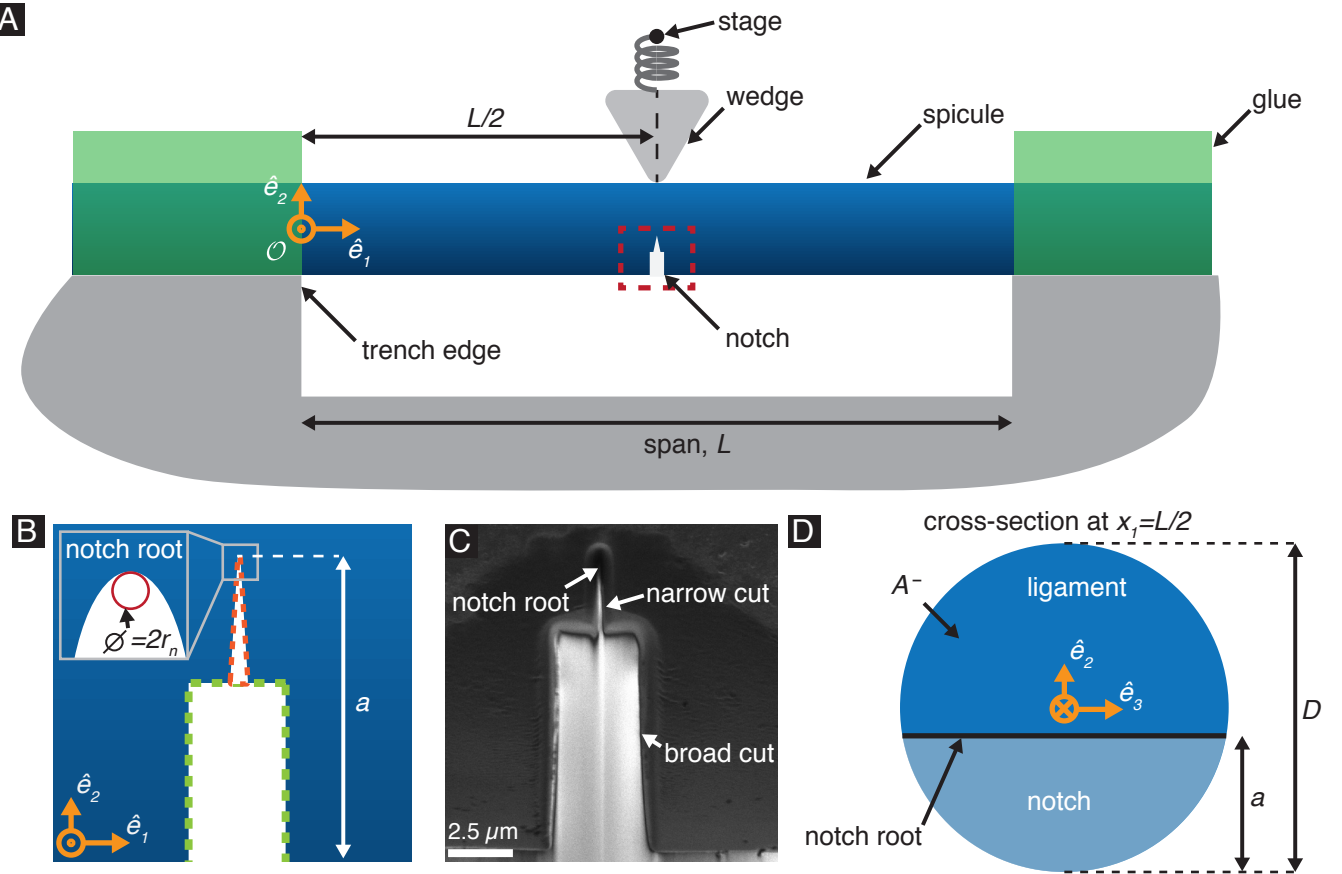


Figure 4. Notched spicule specimen geometry. (A) A schematic of the test configuration. The stage is denoted by a black dot. (B) A magnified view of the region shown in the red rectangle in (A) showing the notch geometry. The broad cut that was made using a high accelerating current is marked in green and the narrow cut that was made using the low accelerating current is marked in orange. (C) A scanning electron micrograph of the notch cut in a representative *Ea*. spicule. (D) A schematic of the spicule's cross-section at $x_1=L/2$ after notching. The notch root is straight and parallel to \hat{e}_3 . The notch length is a . The remaining ligament has a cross sectional area A^- .

97

98 We positioned the spicule underneath a steel wedge so that the apex of the wedge was located at $x_1 = L/2$
99 on the opposite side of the spicule from the notch (see Figure 4 (A)). We used a motorized translation
100 stage to push the wedge into the spicule in $1 \mu\text{m}$ displacement increments at a rate of $1 \mu\text{m/s}$. The
101 displacement of the translation stage is $-w_s \hat{e}_2$ (see Figure 5 (A)). We also measured the displacement
102 of the spicule's cross-section beneath the wedge, w_0 (see Figure 5 (A)). The device used to perform the
103 flexural tests is described in detail in [?, ?]

104 The wedge was attached to a cantilever whose stiffness was measured before the test. We measured
105 the deflection of the cantilever using a fiber optic displacement sensor. The force acting on the spicule

is $-F\hat{e}_2$. We computed F using the cantilever's stiffness and the measured deflection .^[?] Since spicule specimens with longer notches require less force to fracture, we used cantilevers with different stiffnesses depending on the spicule diameter and notch length. The cantilever stiffnesses in our experiments ranged from 88 to 9100 Nm⁻¹.

Our test configuration can be thought of as a modification of the “single edge crack round bar bend” (SEC-RBB) test described by Bush .^[?] In contrast to the standard SEC-RBB test, in our test the specimen's ends are encastered or fixed rather than supported by rollers.

2.1 Force-displacement responses of notched spicules

Representative $F-w_0$ data for an *Ea.* and *Ta.* spicule are shown as dark gray points in Figure 5 (C) and (D), respectively. We observed that F first increases with w_0 up to a value of F_c , at which point there is an abrupt drop in force. We interpret this abrupt drop in force to be the point at which a crack starts growing from the notch root. This event is commonly referred to as “pop-in” .^[?,?] We denote the displacement corresponding to F_c as w_c . The point (w_c , F_c) is shown as a red square in Figure 5 (C) and (D) and the values of w_c and F_c for each specimen are given in Tables S1 and S2.

As we continued to load the spicule after pop-in, the crack propagated across the spicule's cross-section until it completely cleaved the spicule into two pieces. Finally, we unloaded the spicule by moving the stage away from the spicule (i.e., in the \hat{e}_2 direction) in 1 μm displacement increments at a rate of 1 $\mu\text{m s}^{-1}$. The $F-w_0$ data obtained during unloading are shown as light gray points in Figure 5 (C) and (D).

After the spicule was completely unloaded we dissolved the adhesive on its ends and obtained two separate pieces, which we collected for additional imaging (see Section 2.2).

2.2 Fractography

After testing the *Ea.* and *Ta.* spicule specimens, we imaged their fracture surfaces using a scanning electron microscope (see **Figure 6** (A), (B)). In all *Ea.* and *Ta.* specimens, failure appears to occur via a single crack that originates at the notch root. The existence of a single dominant crack is a prerequisite

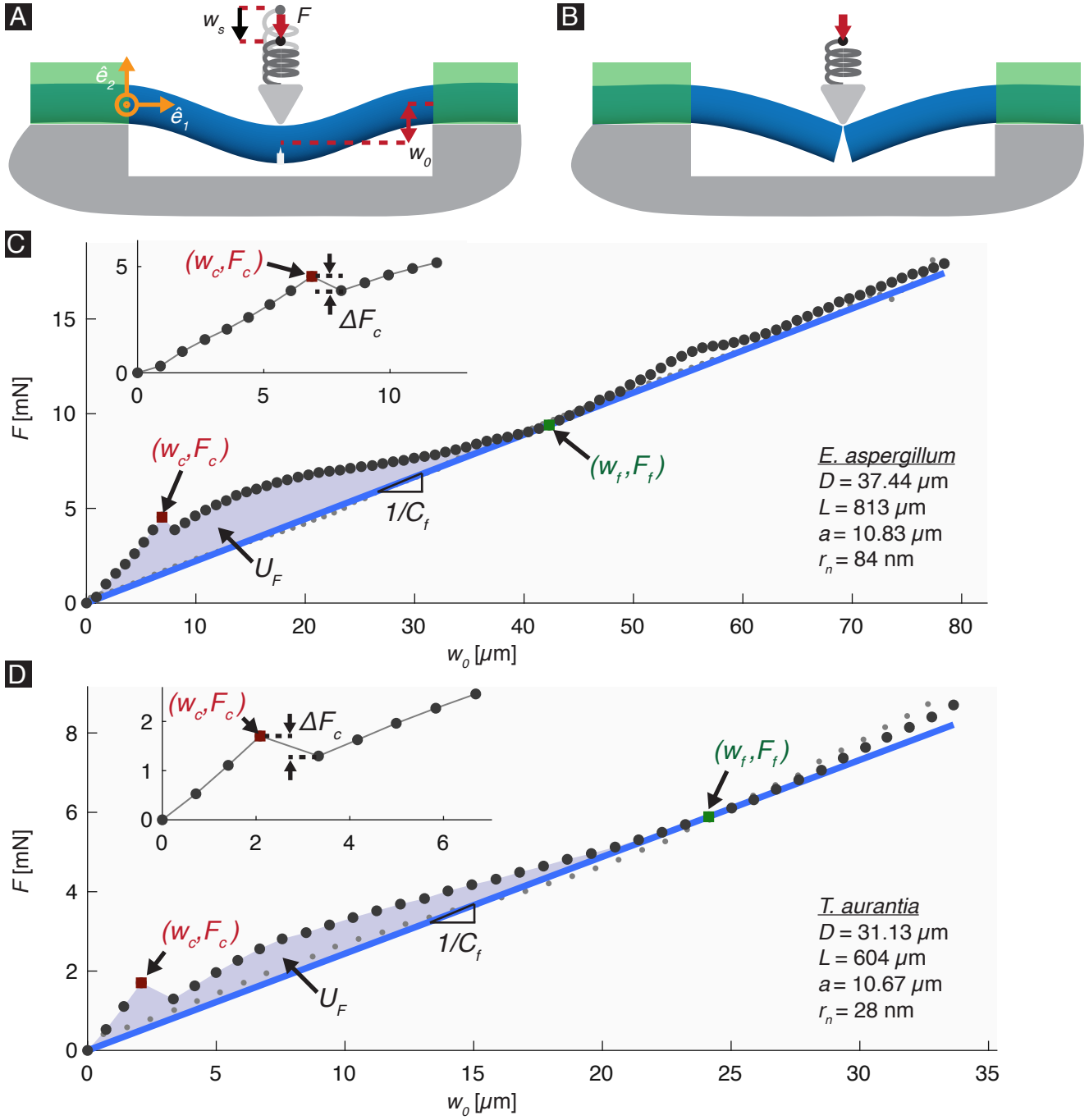


Figure 5. Data obtained from the bending tests. (A) The wedge is used to apply a force $-F\hat{e}_2$. The displacement of the stage is $-w_s\hat{e}_2$ and the corresponding displacement of the spicule's cross-section at $x_1 = L/2$ is $-w_0\hat{e}_2$. The stage is denoted by a black dot. The glue (shown in green) prevents the ends of the spicule from rotating or moving relative to the plate to which it is attached. (B) After the specimen has failed completely, it resembles two cantilevers. (C) The $F-w_0$ response of a representative *Ea*. spicule. (D) The $F-w_0$ response of a representative *Ta*. spicule. The $F-w_0$ data obtained during loading and unloading are shown as dark gray points and light gray points, respectively. Crack initiation (i.e., pop-in) is marked as a red square and has a force and displacement of F_c and w_c . The insets in (C) and (D) show a magnified view of the $F-w_0$ response leading up to pop-in and the drop in force during pop-in, ΔF_c . The point of complete failure is marked with a green square and has a force and displacement of F_f and w_f . The blue line with slope $1/C_f$ is the line that passes through the origin and the point (w_f, F_f) . The shaded region marked U_F in (C) and (D) is the area enclosed between the $F-w_0$ data and this line.

130 to computing the spicules' average crack growth resistance, which we do in Section 2.4.

131 The fracture surfaces of both the *Ea.* and *Ta.* spicules appear to be relatively featureless. In the case of the
132 *Ea.* spicules, this contrasts with the fracture surfaces observed in other SBMs with layered architectures,
133 like nacre and conch shell (see Figure 1 (D), (F)). In these other SBMs the fracture surfaces appear
134 very rough. This roughness is thought to be a signature of the crack arrest and re-nucleation toughening
135 mechanism that occurs when a crack reaches an interface between adjacent layers.^[?, ?, ?, ?] Specifically,
136 after a crack is arrested at an interface between layers, it often will not continue along the same path
137 as before when it re-nucleates in the next layer. The resulting deflection of the crack path manifests
138 as surface roughness in fractographs. As such, the relatively smooth fracture surface of the *Ea.* spicules
139 suggests that they may not possess the same toughening mechanism(s) associated with these other SBMs.

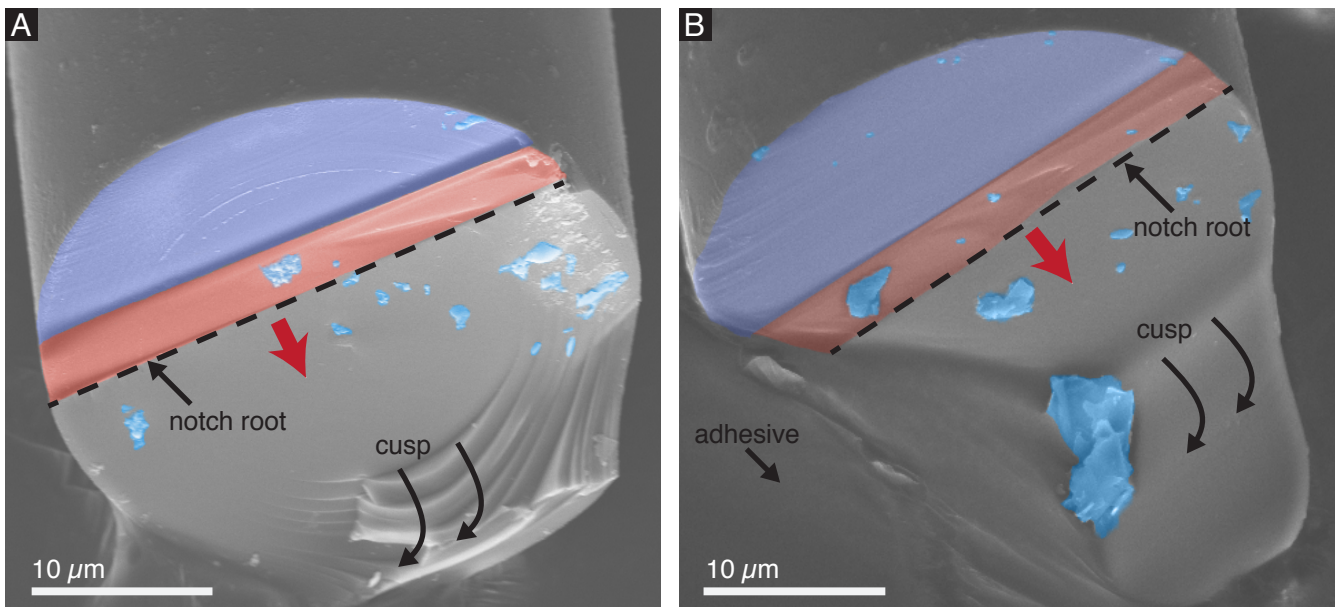


Figure 6. Micrographs of a fractured (A) *Ea.* and (B) *Ta.* spicule. False color is used to mark important features. The purple region in both (A) and (B) corresponds to the coarse (higher current) FIB cut discussed in Section 5.2. The red region in (A) and (B) corresponds to the fine (lower current) FIB cut. The blue regions correspond to debris that we assume collected on the fracture surfaces during specimen preparation. The red arrow denotes the direction of crack growth. The cusp feature in (A) and (B) is a feature of the three-point bending test configuration that appears for both the *Ea.* and *Ta.* spicules. In (B), part of this feature is occluded by the adhesive used to mount the spicule to the aluminum stub.

140

141 The fracture surfaces of both the *Ea.* and *Ta.* spicules have a cusp feature adjacent to where the load is
142 applied (see e.g., Figure 6 (A), (B)). This cusp is characteristic of the three point bending configuration
143^[?] and is a consequence of the compressive stresses caused by the wedge inducing local mixed-mode

144 fracture conditions, which cause the crack to change direction .^[?] The cusp is not a result of a toughening
 145 mechanism caused by the *Ea.* spicules architecture since it also appears in the *Ta.* spicules, which lack
 146 the layered architecture.

147 2.3 Measurements of fracture initiation toughness

148 During pop-in, a crack grows from the notch root in the transverse direction, across the spicule's cross-
 149 section (i.e., in the \hat{e}_2 direction, see Figure 3 (B)). We assume that the crack front is straight and parallel
 150 to the notch root (i.e., parallel to \hat{e}_3) and denote the crack length as Δa . The energy release rate G is given
 151 by

$$G(\Delta a; w_s) = -\frac{1}{2\sqrt{(a + \Delta a)(D - (a + \Delta a))}} \frac{d\Pi(\Delta a; w_s)}{d\Delta a}, \quad (1)$$

152 where $\Pi(\Delta a; w_s)$ is the system's potential energy when the crack's length is Δa and the applied displace-
 153 ment is w_s . For a derivation of Equation (1), see Section S1. It follows from Irwin's analysis of Griffith's
 154 theory of fracture that the necessary condition for crack growth is $G(\Delta a, w_s) \geq R(\Delta a)$, where $R(\Delta a)$ is the
 155 material's crack growth resistance .^[?] We assume that crack growth first occurs when $G(0, w_s) = R(0)$
 156 and w_s is the applied displacement at pop-in. Thus, the fracture initiation toughness $R(0)$ is given by

$$R(0) = -\frac{1}{2\sqrt{a(D-a)}} \left. \frac{d\Pi(\Delta a; w_s)}{d\Delta a} \right|_{\Delta a=0}, \quad (2)$$

157 where w_s is the applied displacement at pop-in.

158 For each *Ea.* and *Ta.* spicule that we mechanically tested, we measured $R(0)$ by computing the derivative
 159 in Equation (2) using a computational mechanics model. This model is described in detail in Section
 160 S3. In the computational mechanics model we consider both the *Ea.* and *Ta.* spicules to be made of a
 161 homogeneous, linear elastic material. In reality, the *Ea.* spicules contain layers and are therefore not
 162 homogeneous. Therefore, the values of $R(0)$ that we obtain for the *Ea.* spicules should be considered to
 163 be an *effective* fracture initiation toughness.

164 The accurate estimation of $R(0)$ using Equation (2) is predicated on the assumption that the notch be-
 165 haves like a sharp crack (i.e., the radius of curvature of the notch root is vanishingly small). It has been

166 shown that the FIB cutting technique can produce notch root radii that are small enough to act like sharp
167 cracks .^[?] This is supported by additional work ^[?] showing that if the notch root radius is less than
168 twice the smallest microstructural length scale, then the measured value of $R(0)$ becomes insensitive to
169 the notch root geometry. The *Ea.* spicules' layers are composed of silica nanoparticles that are approxi-
170 mately 100 nm in diameter .^[?] We take the size of these nanoparticles to be the smallest microstructural
171 length scale present in the *Ea.* spicules. We assume that the *Ta.* spicules have a similar smallest mi-
172 crostructural length scale. This assumption is supported by atomic force microscopy of the *Ta.* spicules
173 .^[?] Therefore, in order for the value of $R(0)$ to be insensitive to the notch root geometry, the radius of
174 curvature of the notch root, r_n , should be less than 200 nm (see Figure 4 (B) inset).

175 We measured r_n for each specimen from scanning electron micrographs by manually selecting three
176 points along the profile of the notch root and fitting a circle to these points (see Tables S1 and S2).
177 The mean value±standard error of r_n for the 35 *Ea.* spicules and 26 *Ta.* spicules was 112±14 nm and
178 149±15 nm, respectively. We identified 4 *Ea.* spicule specimens and 5 *Ta.* spicule specimens for which
179 r_n exceeded 200 nm, and consequently we did not compute $R(0)$ for these specimens. Additionally, there
180 were 9 *Ea.* spicule specimens for which we were unable to reliably identify the pop-in event by inspecting
181 the F - w_0 response, and therefore could not obtain w_c . Thus, we computed $R(0)$ for 22 *Ea.* spicules and
182 21 *Ta.* spicules (see **Figure 7 (A)**).

183 We measured $R(0)$ for the *Ta.* spicules to be 3.76±0.49 Jm⁻² (mean±standard error, $N = 21$) and $R(0)$
184 for the *Ea.* spicules to be 7.15±1.83 Jm⁻² (mean±standard error, $N = 22$). The measurements of $R(0)$
185 for each spicule are shown in Figure 7 (A) and in Tables S1 and S2. Overall, these values are similar
186 to those expected for glass and other brittle ceramic materials (see Figure 7 (A)). In the case of the *Ta.*
187 spicules, the value of $R(0)$ appeared relatively constant regardless of the dimensionless notch length,
188 $\alpha = a/D$. For values of $\alpha > 0.1$, the fracture initiation toughness of the *Ea.* spicules was also relatively
189 constant. However, the *Ea.* spicules displayed a sharp increase in $R(0)$ for $\alpha < 0.1$ (see Figure 7 (A)). The
190 largest value of $R(0)$ that we measured was 33.84 Jm⁻² for an *Ea.* spicule specimen with $\alpha=0.07$. The
191 increase in fracture initiation toughness for small values of α suggests that the *Ea.* spicule's architecture
192 is increasing its effective fracture initiation toughness for small flaws or cracks.

193 We offer the following qualitative explanation for this observed increase in $R(0)$. Recall that the *Ea.*

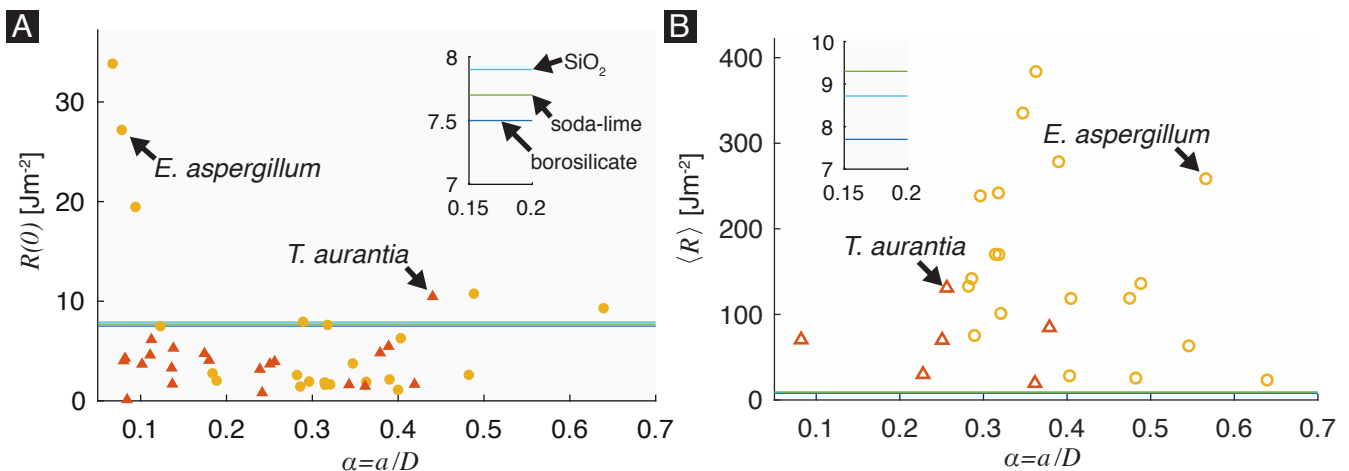


Figure 7. Crack growth resistance of *Ea.* and *Ta.* spicules. (A) Fracture initiation toughness, $R(0)$, of 22 *Ea.* spicules (yellow circles) and 21 *Ta.* spicules (red triangles) versus dimensionless notch length, $\alpha = a/D$. Reference lines are shown corresponding to the fracture initiation toughnesses of three types of synthetic glass measured by .^[?] The inset shows a closer view of these three values. (B) Average crack growth resistance, $\langle R \rangle$, of 19 *Ea.* spicules (hollow yellow circles) and 6 *Ta.* spicules (hollow red triangles) versus α . Reference lines are given that correspond to the average crack growth resistance of the three types of synthetic glass shown in (A). We computed the value of $\langle R \rangle$ from the measurements of the work of fracture provided by .^[?] The inset in (B) shows a closer view of these three values.

spicule's cross-section consists of ≈ 25 cylindrical layers surrounding a large, monolithic core. In a previous work, it was shown that the ratio of the core's diameter to the spicule's diameter is relatively constant with a mean value of 0.41 and a standard deviation of 0.07 ($N=116$) .^[?] From this it can be shown that the value of α at which the notch reaches the core of the spicule is approximately 0.3. Thus, for $\alpha < 0.3$ a crack growing from the notch will initially propagate perpendicular to some of the interlayers. It has been shown that when a crack propagates perpendicular to the spatial variation of material properties in a structure consisting of flat layers of a stiff material that are separated by thin, compliant or weak interlayers, the structure will display enhanced fracture initiation toughness compared to the bulk material .^[?, ?, ?] The toughness enhancement is a result of the energy release rate decreasing when a crack impinges on a compliant or weak interlayer .^[?, ?] This mechanism has been observed experimentally in bioinspired composites .^[?, ?] and previous works have speculated that it may also operate in the *Ea.* spicules .^[?, ?] Our observation that $R(0)$ increases with decreasing α is consistent with the predictions of these models .^[?, ?, ?] For specimens with $\alpha > 0.3$, the notch reaches the silica core of the spicule where there are no interlayers, and the interlayers between the silica layers outside the core are not perpendicular to the initial direction of crack growth. Therefore, in these specimens the spicule would not be able to benefit from the above-mentioned toughness enhancement mechanism. In agreement with this

210 observation, in the *Ea.* spicules with $\alpha > 0.3$, the values of $R(0)$ are similar to those that we measured in
211 the *Ta.* spicules (see Figure 7 (A)).

212 2.4 Measurements of average crack growth resistance

213 In our experiment the average crack growth resistance, $\langle R \rangle$ is defined as

$$\langle R \rangle = \frac{1}{D-a} \int_0^{D-a} R(\Delta a) d\Delta a. \quad (3)$$

214 We measured $\langle R \rangle$ using the work of fracture method .^[?,?] Specifically, it can be shown that

$$\langle R \rangle = 2\gamma_{WOF}, \quad (4)$$

215 where γ_{WOF} is called the work of fracture .^[?] The work of fracture is obtained by fracturing a specimen,
216 measuring the total energy that is consumed by the fracture process, U_F , and dividing that by the total
217 new surface area created .^[?] Because the spicule specimens are cleaved into two pieces by a single crack
218 emanating from the notch root (see Section 2.2), we take the total new surface area created to be twice
219 the cross-sectional area of a specimen's ligament before any crack growth has occurred, A^- (see Figure 4
220 (D)). Therefore, $\langle R \rangle$ is given by

$$\langle R \rangle = U_F/A^-. \quad (5)$$

221 In order to compute $\langle R \rangle$ using Equation (5), the crack must grow in a stable manner throughout the test
222 .^[?,?] Unstable crack growth events appear as discontinuities in the $F-w_0$ response. The pop-in (marked
223 by a red square in Figure 5 (C) and (D)), is an example of such an event. Consequently, $\langle R \rangle$ computed
224 using Equation (5) from the $F-w_0$ data will be an overestimate of the actual value of $\langle R \rangle$. Aside from the
225 pop-in event, however, the $F-w_0$ curves shown in Figure 5 are continuous. For that reason, we believe that
226 in our experiments the cracks grow in a predominantly stable manner. Previous studies have attempted
227 to compute the spicule's work of fracture from their $F-w_0$ response .^[?,?] However, the data presented in
228 these previous studies suggests that the crack growth was not stable and therefore the data in these studies

229 cannot be used to obtain accurate estimates of $\langle R \rangle$.

230 We used the magnitude of the drop in F at pop-in as a criterion for determining which spicule specimens
231 could be used to estimate $\langle R \rangle$. Specifically, we measured the drop in force during pop-in, ΔF_c (see Figure
232 5 (C), (D) inset), and compared it to F_c . We considered a test to have predominantly stable crack growth
233 if $\Delta F_c \leq 0.15F_c$. We identified 16 *Ea.* and 20 *Ta.* spicules for which $\Delta F_c > 0.15F_c$ and consequently we
234 could not compute $\langle R \rangle$ for these specimens.

235 If the crack grows in a predominantly stable manner then the change in kinetic energy of the spicule
236 during the test is negligible and it can be shown that

$$U_F + U_{ef} = \int_0^{w_f} F dw_0, \quad (6)$$

237 where w_f is the value of w_0 at which the crack has just cleaved the specimen into two pieces and U_{ef}
238 is the elastic energy of the spicule in the completely failed state. The integral on the right hand side
239 of Equation (6) is the work done on the spicule until it has completely failed. In order to evaluate this
240 integral we must identify the (w_0, F) point at which the crack had just cleaved the spicule into two pieces.

241 We assume that if at any point during the test we were to unload the spicule, F would decrease linearly
242 with w_0 until the values of both reached zero. Our rationale for this assumption is that the spicule
243 behaves in a linear elastic fashion when there are no dissipative processes operating (e.g., crack growth).
244 This means that the elastic unloading compliance of the spicule at a point (w_0, F) is given by $C = w_0/F$.
245 Since crack growth invariably increases the elastic unloading compliance of a structure, we know that C
246 should be greatest when the crack has completely cleaved the spicule into two pieces. Thus, we define
247 w_f and the corresponding force, F_f , at which the spicule has just been cleaved into two pieces to be the
248 (w_0, F) point for which C is maximum. The point (w_f, F_f) is shown in Figure 5 (C) and (D) as a green
249 square. The line with slope $1/C_f$ that passes through both this point and the origin is also shown in
250 Figure 5 (C) and (D) in blue. The values of w_f and F_f for each specimen are given in Tables S1 and S2.

251 In many test configurations, such as the standard single edge crack specimen ,^[?] $U_{ef} = 0$. However, for
252 the configuration that we use, U_{ef} is nonzero since the specimen's stiffness is finite even after the crack
253 has completely cleaved the specimen into two halves. Specifically, when our specimen has completely

254 failed, the elastic energy is given by $U_{ef} = w_f F_f / 2$. We can therefore simplify Equation (5) and (6) to
 255 get

$$\langle R \rangle = \frac{\int_0^{w_f} F dw_0 - w_f F_f / 2}{A^-}. \quad (7)$$

256 For a specimen with a circular cross-section containing a notch of length a and crack of length Δa , as
 257 shown in Figure 3 (B), the area of the intact portion of the specimen's cross-section is

$$A(\Delta a) = \frac{\pi D^2}{4} + \frac{1}{2} (D - 2(a + \Delta a)) \sqrt{(a + \Delta a)(D - (a + \Delta a))} - \frac{D^2}{4} \cos^{-1} \left(1 - \frac{2(a + \Delta a)}{D} \right). \quad (8)$$

258 In Equation (8) we assume that both the notch root and crack front are straight line segments that are
 259 parallel to \hat{e}_3 . We computed $A^- = A(0)$ from Equation (8) using the a and D that we measured from
 260 scanning electron micrographs taken before the flexural tests (see Section 2).

261 For 19 *Ea.* and 6 *Ta.* spicule specimens we computed $\langle R \rangle$ from Equation (7) using trapezoidal integration
 262 of the F - w_0 data up to the point (w_f, F_f) . We found $\langle R \rangle$ to be $160.12 \pm 23.99 \text{ J m}^{-2}$ (mean \pm standard error,
 263 $N=19$) and $67.56 \pm 16.37 \text{ J m}^{-2}$ (mean \pm standard error, $N=6$) for the *Ea.* and *Ta.* spicules, respectively. The
 264 measurements of $\langle R \rangle$ for each spicule are shown in Figure 7 (B) and in Tables S1 and S2.

265 2.5 Comparison of toughness enhancements

266 We found that average crack growth resistance of the *Ea.* spicules was higher than that of the *Ta.* spicules.
 267 Specifically, computing the ratio $\langle R \rangle^{(\text{EA})} / \langle R \rangle^{(\text{TA})}$ shows that the architecture increases $\langle R \rangle$ by a factor of
 268 2.37. While this ratio is evidence that the *Ea.* spicule's architecture does enhance toughness, we should
 269 put this enhancement in the context of enhancements observed in other SBMs. We denote the crack
 270 growth resistances of an architected material and its corresponding homogeneous ceramic constituent
 271 with the superscripts (arch) and (hom), respectively. By computing $\langle R \rangle^{(\text{arch})} / \langle R \rangle^{(\text{hom})}$ for nacre, bone,
 272 antler and conch shell using work of fracture data available from literature (see **Figure 8 (B)** and Table 2),
 273 we see that the $\langle R \rangle$ enhancement in the *Ea.* spicules is quite small. For example, $\langle R \rangle^{(\text{arch})} / \langle R \rangle^{(\text{hom})}$ for
 274 the conch shell exceeds 1000; several hundred times larger than the $\langle R \rangle$ enhancement in the *Ea.* spicules.

275 By computing the enhancement in $R(0)$ using the same procedure, we see that $R(0)^{(\text{arch})} / R(0)^{(\text{hom})}$ can

276 be as large as \approx 200 in these other biological materials (see Figure 8 (A)). In contrast, we measured
277 $R(0)^{(\text{arch})}/R(0)^{(\text{hom})}$ to be only 1.90 for the *Ea.* spicules on average. Even when considering the relatively
278 large increase in $R(0)$ for short notches (see Section 2.3 for details), the maximum enhancement that we
279 observed is on the order of 10. While this increase is similar to those observed in conch and antler it still
280 is quite small compared to nacre—often considered the archetype for tough biological materials. Thus,
281 while the *Ea.* spicules share a common architectural motif with many tough SBMs, our measurements
282 suggest that these seemingly similar architectures do not provide comparable enhancements to either the
283 fracture initiation toughness or average crack growth resistance.

284 Other studies have compared the mechanical behaviors of spicules with layered architecture to synthetic
285 glass fibers ,^[?, ?, ?, ?, ?] despite the spicules having a lower elastic modulus and a different chemical compo-
286 sition .^[?, ?, ?] Unlike synthetic glass, the *Ea.* spicules are composed of hydrated silica that is precipitated
287 onto a proteinaceous scaffold .^[?] The effect of this scaffold on the mechanical properties of the spicule’s
288 silica is not fully understood. It would therefore not be possible to isolate the effect of the spicule’s
289 layered architecture on its toughness properties by comparing them to synthetic glass fibers. The *Ea.*
290 spicules should instead be compared to a specimen composed of the same biogenic silica but which is
291 monolithic. An ideal choice for this homogeneous control material would be a section of the solid silica
292 core of the *Ea.* spicules. However, so far we have not successfully obtained a large enough section of the
293 *Ea.* spicule core to perform fracture tests. Therefore, we chose the *Ta.* spicules as what we believe to be
294 the next best alternative.

295 3 Discussion

296 Toughness enhancements in SBMs are often caused by multiple mechanisms that are triggered as a crack
297 interacts with the features of the material’s architecture .^[?, ?, ?] For example, in nacre and other mollusk
298 shells one important toughening mechanism is crack arrest .^[?, ?, ?] This phenomenon occurs when a crack
299 impinges on a weak interface between two layers and requires more energy to resume propagation in the
300 adjacent, undamaged layer. Often, the arrest of a crack will be accompanied by crack deflection along the
301 interface between the adjacent layers. Based on the jagged fracture surfaces observed in previous studies

Table 2. Summary of SBM crack growth resistance data used to compute the toughness metrics in Figure 8. Statistical data, such as standard deviation (s.d.) standard error (s.e.) and sample number (N) are included when available.

Material	$R(0)$ [Jm $^{-2}$]	$\langle R \rangle$ [Jm $^{-2}$] ^{c)}	Ref.
nacre (<i>Pinctada margaritifera</i>)	587 \pm 189 (mean \pm s.d., N =14)	2068 \pm 544 (mean \pm s.d., N =12)	[?]
nacre (<i>Pinctada margaritifera</i>)	—	3300 \pm 78 (mean \pm s.e.) ^{d)}	[?]
nacre (<i>Pinctada margaritifera</i>)	—	2880 \pm 260 (mean \pm s.d.) ^{d)}	[?]
bone (<i>Homo sapiens</i>)	50–200	11250 ^{e)}	[?]
bone (<i>Homo sapiens</i>)	224 \pm 2 (mean \pm s.d., N =7) ^{f)}	—	[?]
bone (<i>Papio anubis</i>)	—	15520 \pm 2900 (mean \pm s.d., N =3)	[?]
bone ^{a)}	—	8000 \pm 524 (mean \pm s.e.) ^{d)}	[?]
antler (<i>Cervus canadensis</i>)	100 ^{e)}	14000 ^{e)}	[?]
conch (<i>Strombus gigas</i>)	25 \pm 7 (mean \pm s.d., N =4)	26000 \pm 14000 (mean \pm s.d., N =8)	[?]
calcite ^{b)}	\approx 3	—	[?]
limestone	—	22	[?]
hydroxyapatite ^{b)}	\approx 10	—	[?]
hydroxyapatite	—	140	[?]

^{a)} The authors of this work did not specify the genus and species from which the bone specimens were obtained;

^{b)} Approximate values are given because the data was taken from a graph showing ranges of property values;

^{c)} Values were obtained for the work of fracture, γ_{WOF} , and were used to compute $\langle R \rangle = 2\gamma_{WOF}$;

^{d)} The number of specimens was not given in the referenced work;

^{e)} Values estimated from R -curve data;

^{f)} The reference provides the mode I stress intensity factor, K_I , at crack growth initiation. From this we estimated $R(0)$ to be K_I^2/E , where E is the Young's modulus .^[?] We take the value of E to be 18.6 GPa as per .^[?]

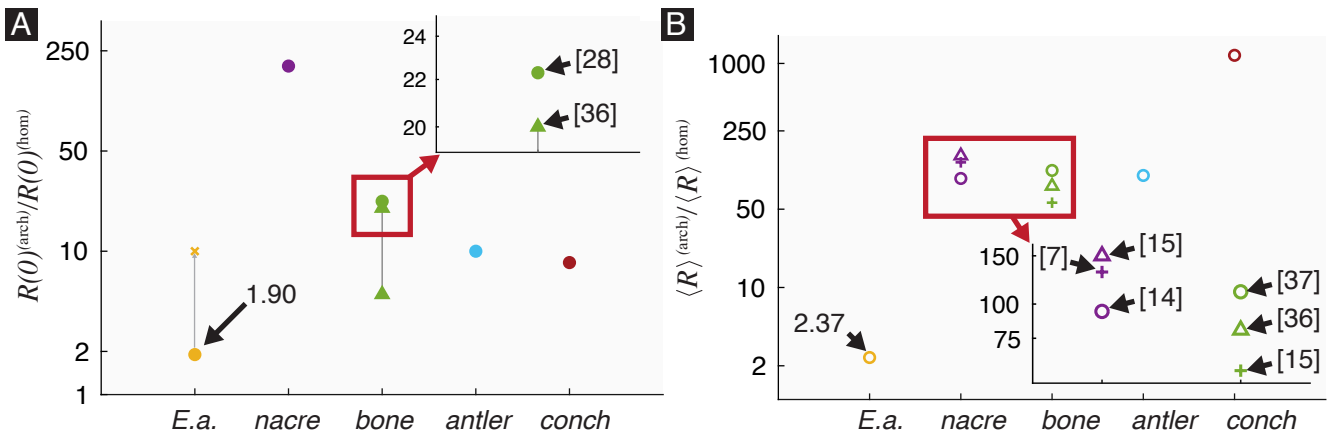


Figure 8. Comparison of the *Ea.* spicule's toughness enhancement to the toughness enhancements of other SBMs with layered architectures. (A) The initiation toughness enhancement metric $R(0)^{(\text{arch})}/R(0)^{(\text{hom})}$ of the *Ea.* spicules and other SBMs with layered architectures. We used the value $R(0)^{(\text{hom})} = 3 \text{ Jm}^{-2}$ of calcite as the control material for nacre and conch ,^[?] and $R(0)^{(\text{hom})} = 10 \text{ Jm}^{-2}$ of hydroxyapatite ^[?] as the control material for bone and antler. For *Ea.*, the solid circle represents the average and the cross represents the approximate value of the maximum enhancement which we observed for very short notches.(B) The average toughness enhancement metric $\langle R \rangle^{(\text{arch})}/\langle R \rangle^{(\text{hom})}$ of the *Ea.* spicules and other SBMs with layered architectures. We used the value $\langle R \rangle^{(\text{hom})} = 11 \text{ Jm}^{-2}$ of limestone as the control material for nacre and conch ,^[?] and $\langle R \rangle^{(\text{hom})} = 70 \text{ Jm}^{-2}$ of hydroxyapatite ^[?] as the control material for bone and antler. In both (A) and (B), the values of $R(0)$ and $\langle R \rangle$ for nacre, bone, antler, and conch (*S. gigas*) were obtained from the literature (see Table 2). The multiple values for bone in (A) and for nacre and bone in (B) correspond to experiments performed by different research groups. The two green triangles connected by a line in (A) correspond to the range of values reported by .^[?] The references from which the data points were obtained are annotated in the insets. Note that in both (A) and (B) the toughness enhancement metrics are plotted using a logarithmic scale.

of *Ea.* spicules (see Figure 2 (C)), it has been speculated that the spicules *may* also benefit from toughening through crack arrest and re-nucleation .^[?,?] However, the fracture surfaces of the notched spicules (see Section 2.2) are relatively featureless (see Figure 6 (A)). From these results and the relatively small toughness enhancement observed in the *Ea.* spicules it is clear that the *Ea.* spicule's architecture does not trigger the same toughening mechanisms observed in these other SBMs. Or, if the same toughening mechanisms are triggered, they are not as effective in the *Ea.* spicules.

To understand the difference between the toughening mechanisms operating in the *Ea.* spicules and in SBMs like nacre we performed virtual experiments using a regularized variational fracture (RVF) method (see Section S4 for details). These virtual experiments allowed us to predict the mechanical behaviors of and crack paths in materials with layered architectures. Specifically, we used the RVF method to simulate crack growth in a material with flat/planar layers, like those which appear in nacre, and a material with cylindrical layers, like in the *Ea.* spicules.

Our model material with a planar layered architecture consists of a notched beam with a rectangular cross-

315 section whose width $W = 1$ mm, thickness $H = 1$ mm and length $L = 5$ mm. The beam is composed
316 of two layers separated by a thin “interlayer” (see **Figure 9 (A)**). Similarly, our model material with a
317 cylindrical layered architecture consists of a notched beam with a cylindrical cross-section composed of
318 two layers separated by a cylindrical interlayer (see Figure 9 (B)). We constrained the cylindrical beam
319 to have the same volume as the rectangular beam and therefore its diameter $D = 1.12838$ mm and length
320 $L = 5$ mm. The notch length a in both beams is 0.2 mm.

321 In both beams, the interlayer has a thickness $t = 0.1$ mm and is located a distance $b = 0.2$ mm from the
322 notch root. The Young’s modulus $E = 20.8$ GPa and Poissons ratio $\nu = 0.3$ are the same in both the
323 layers and the interlayer. However, the fracture toughness is $G_b = 500 \text{ Jm}^{-2}$ in the layers and $G_I = 0.5$
324 Jm^{-2} in the interlayer. We loaded the beams in three-point bending by applying a displacement w_0 shown
325 in Figure 9.

326 In Figure 9 (C) we show the load-displacement ($F-w_0$) response of the planar layered beam as well as that
327 of a beam with the same geometry but without the interlayer. The monolithic beam exhibits typical brittle
328 behavior with crack initiation occurring at $F \approx 25$ N leading to a large drop in F , which corresponds to
329 abrupt crack growth, followed by a decrease in F until complete failure. The planar layered beam shows
330 an almost identical response until the peak load is reached and first load drop occurs. After the first load
331 drop, however, the load again increases before a second load drop occurs leading to complete failure.
332 The crack path for the planar layered beam at $w_0 = 0.16$ mm is shown in Figure 9 (D). By examining the
333 crack path at different values of w_0 , we observe three stages of crack growth:

- 334 1. A crack initiates at the peak load and grows until it reaches the interlayer. This corresponds to the
335 first load drop from $F \approx 25$ N to $F \approx 9$ N. Once the crack reaches the interlayer, it is arrested.
- 336 2. The load then increases from $F \approx 9$ N to $F \approx 10$ N. During this increase, some amount of interfacial
337 fracture occurs (see Figure 9 (D)) but the crack does not grow into the second layer. Thus, the
338 increase in load corresponds to the crack being arrested by the weak interface.
- 339 3. Finally, the crack re-nucleates in the second layer, resulting in the second load drop from $F \approx 10$ N
340 to $F \approx 5$ N. After the second load drop, the crack continues to grow through the second layer until
341 complete failure occurs.

342 We computed $\langle R \rangle^{(\text{arch})} / \langle R \rangle^{(\text{hom})}$ from the force-displacement response of the planar layered beam to be
 343 1.18. This toughness enhancement is caused by the combined effects of two toughening mechanisms:
 344 interfacial fracture, and crack arrest and re-nucleation.

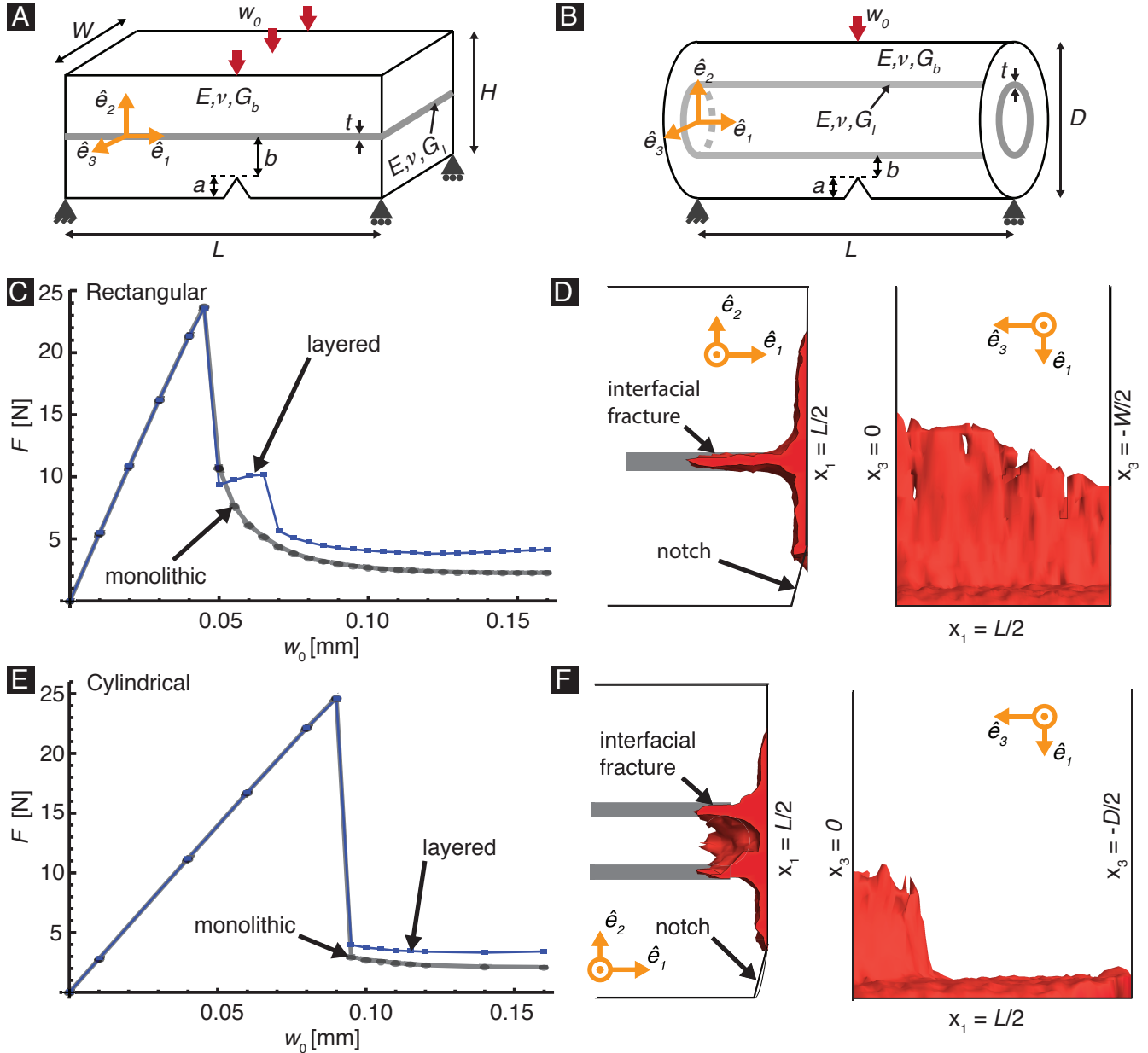


Figure 9. Regularized variational fracture model of beams with planar and cylindrical layered architectures. (A) Geometry of the notched layered beam with one planar interlayer shown in gray. (B) Geometry of the notched cylindrical layered beam with one cylindrical interlayer shown in gray. (C) Load displacement ($F-w_0$) response of the planar layered beam loaded in three-point bending. (D) Crack paths in the planar layered beam as seen from the planes whose normal vectors are \hat{e}_3 and \hat{e}_2 . The red region corresponds to the crack path predicted by the RVF calculations at a displacement $w_0 = 0.16$ mm. (E) $F-w_0$ response of the cylindrical layered beam loaded in three-point bending. (F) Crack paths in the cylindrical layered beam as seen from the planes whose normal vectors are \hat{e}_3 and \hat{e}_2 . The red region corresponds to the crack path predicted by the RVF calculations at a displacement $w_0 = 0.16$ mm. The gray curves in (C) and (E) correspond to monolithic beams with the same geometry and bulk properties.

345 In the case of the cylindrical layered beam, we observed that the F - w_0 response is almost identical to that
346 of its corresponding monolithic beam (see Figure 9 (E)). By examining the crack path for the cylindrical
347 layered beam at different values of w_0 (e.g., see Figure 9 (F)) we observed that interfacial fracture occurs
348 to roughly the same extent as in the planar layered beam. This results in a small toughness enhancement,
349 $\langle R \rangle^{(\text{arch})} / \langle R \rangle^{(\text{hom})}$, of 1.05. However, unlike the planar layered beam, the crack does not become arrested
350 at the interlayer. The absence of the crack arrest and re-nucleation toughening mechanism explains
351 why the toughness enhancement in the cylindrical layered beam is substantially lower than in the planar
352 layered beam.

353 From this we conclude that while interfacial fracture does enhance the toughness of the cylindrically lay-
354 ered beam, its effect is small compared to the arrest and re-nucleation mechanism that occurs in the planar
355 layered beam. This difference in toughening mechanisms could explain why the toughness enhancement
356 is so much smaller for the *Ea.* spicules than for other SBMs with planar layered architectures.

357 4 Conclusion

358 The surprisingly limited toughness enhancement provided by the *Ea.* spicule's architecture reminds us
359 that it is important to measure each SBM's toughness properties rather than categorizing it as tough solely
360 based on the existence of a layered architecture. Furthermore, the contrast between our findings and
361 previous speculations that the *Ea.* spicule's layers enhance their toughness shows that the understanding
362 of the relationship between layered architectures and toughness enhancement is not yet complete. By
363 showing the extreme variability of the toughness enhancements that are provided by different layered
364 architectures (see Section 2.5 and Figure 8), we hope to galvanize interest in developing a more complete
365 understanding of this relationship. A better understanding of this structure-property relationship is crucial
366 for developing useful bio-inspired designs and avoiding the pitfalls of naive biomimicry.

367 **5 Methods**

368 **5.1 Spicule specimen preparation**

369 *Euplectella aspergillum* skeletons were received dried with the organic tissue removed (see Figure 2 (A)).

370 We removed spicules from the basal portion of the skeleton using tweezers and cut \approx 5 mm sections from

371 roughly the midpoint along their length using a razor blade. *Tethya aurantia* spicules were received dried

372 and separated from the sponge's organic tissue. We inspected the *Ea.* and *Ta.* spicules using a polarized

373 light microscope and discarded specimens that were visibly cracked or damaged.

374 All specimens were stored in dry conditions prior to testing. We are aware that the mechanical properties

375 of some SBMs can change substantially if they are soaked in water before testing. For example, the work

376 of fracture of nacre that has been soaked in artificial seawater is 137% higher than that of the same nacre

377 stored in dry conditions .^[?] The soaking procedure is thought to restore the organic phases within them

378 to their native, hydrated state. However, in Supplementary Information S2, we compare the Young's

379 modulus and bending failure strain of *Ea.* spicule specimens stored in wet and dry conditions and find

380 no significant difference between the two (see Supplementary Information S2 for statistical analysis).

381 Motivated by these results, we chose to test the spicules in their as-received, dry state.

382 **5.2 Spicule notching procedure**

383 We cut notches in the spicules using a focused ion beam (FIB) and a procedure similar to that described

384 in .^[?] Before notching, we coated the spicules in 10 nm of carbon to prevent charge accumulation during

385 the cutting procedure. We cut each notch in two steps. First, we used a relatively large accelerating

386 current of 6.5 nA at 30 kV to make a broad cut (marked schematically in green in Figure 4 (B)). Then,

387 we used a lower accelerating current of 460 pA at 30 kV to make a narrower cut (marked schematically

388 in orange in Figure 4 (B)). The FIB was programmed to make the broad cut between 1.5 and 3 μ m wide

389 depending on the desired depth of the notch. Deeper notches required wider cuts in order to prevent the

390 material that was ablated by the FIB from redepositing on the specimen. The narrow cut was programmed

391 to be 250 nm wide.

392 The actual widths of the cuts differed from these programmed values because the ion beam has a finite
393 width. For each *Ea.* and *Ta.* spicule, we directly measured the widths of both the broad and narrow cuts
394 from scanning electron micrographs (see e.g., Figure 4 (C)). Specifically, we measured the width of a
395 cut at the points located closest to and furthest from the notch root. We then averaged the measurements
396 taken at these two points and took this average value to be the width of the cut. Using this procedure
397 we measured the broad cuts to be 3.58 ± 0.24 μm wide and the narrow cuts to be 501 ± 21 nm wide
398 (mean \pm standard error, $N = 61$; 35 of which were *Ea.* spicules and 26 of which were *Ta.* spicules).

399 This two step cutting process and the resulting notch geometry is similar to the procedure for preparing
400 standard edge-notch bending specimens in which a notch is first cut using a diamond saw (broad cut) and
401 then subsequently scored using a razor blade (narrow cut). [?, ?, ?]

402 Focused ion beams (FIBs) have previously been used to cut notches in micrometer-scale fracture spec-
403 imens. [?, ?, ?, ?] One concern about this technique is that the cutting mechanism—i.e., material ablation
404 using gallium ions—can cause gallium ion implantation. This implantation alters local composition of
405 the material and therefore could affect the local material properties near the notch root. Furthermore, ion
406 implantation could result in the generation of compressive stresses within the material, which may have
407 an effect on the measured fracture initiation toughness. A previous study [?] addressed these concerns by
408 measuring the fracture initiation toughness of silicon (100) using FIB notched specimens and comparing
409 these measurements to values obtained by other research groups that used macroscopic specimens and
410 alternative notching procedures. [?] Their results also match those obtained from fracture tests performed
411 on single crystal silicon specimens that were pre-cracked using a Knoop indenter and loaded in four-point
412 bending. [?] Thus, they demonstrate that ion implantation does not appear to affect the measurement of
413 fracture initiation toughness.

414 **Acknowledgements** We thank James Weaver for providing us with the *Ta.* spicules and Jarod Ferreira
415 for his help constructing the mechanical testing device. **We thank the reviewers of this paper for their**
416 **insightful comments that led us to connect the observed increase in fracture initiation toughness with**
417 **decreasing notch length to previous models describing toughness enhancement in materials with layered**
418 **architectures (Section 2.3)** This work was supported by National Science Foundation [Mechanics of
419 Materials and Structures Program, grant number 1562656]; and the American Society of Mechanical
420 Engineers [Haythornthwaite Research Initiation Grant]. M.A.M. received additional support from the
421 NASA Rhode Island Space Grant Consortium.

422 **Author Contributions** M.A.M. and S.K. designed and performed the fracture tests. M.A.M. analyzed
423 the data. K.V. developed the computational fracture mechanics models of the spicules. H.K. designed
424 the research. M.A.M., K.V. and H.K. wrote the paper. All authors discussed the results and commented
425 on the manuscript.

426 **Author Information** Correspondence and requests for materials should be addressed to
427 H. K. (haneesh_kesari@brown.edu).

428 **Competing Financial Interests** The authors declare no competing financial interests.

429 Supplementary Information

430 **Architecture in Stiff Biological Materials: a Template for Toughness Enhancement, or a Siren
431 Song?**

432 *Michael A. Monn, Kaushik Vijaykumar, Sayaka Kochiyama, and Haneesh Kesari**

1 **S1 Derivation of the equation for fracture initiation toughness**

2 The energy release rate at an applied displacement w_s and crack length Δa is given by

$$G(\Delta a; w_s) = -\frac{d\Pi(\Delta a; w_s)}{d\Delta A}, \quad (\text{S1})$$

3 where ΔA is the area of the crack. For a specimen with a circular cross-section containing a notch of
4 length a and crack of length Δa , the intact area of the specimen's cross-section $A(\Delta a)$ can be computed
5 using Equation (8). The area of the crack is then given by

$$\Delta A(\Delta a) = A(0) - A(\Delta a). \quad (\text{S2})$$

6 Consequently, we can rewrite Equation (S1) as

$$\begin{aligned} G(\Delta a; w_s) &= -\frac{d\Pi(\Delta a; w_s)}{d\Delta a} \left(\frac{d\Delta A(\Delta a)}{d\Delta a} \right)^{-1} \\ &= -\frac{1}{2\sqrt{(a + \Delta a)(D - (a + \Delta a))}} \frac{d\Pi(\Delta a; w_s)}{d\Delta a}, \end{aligned} \quad (\text{S3})$$

7 Per Irwin's analysis of Griffith's theory of fracture, the necessary condition for the extension of a crack is

$$G(\Delta a; w_s) \geq R(\Delta a), \quad (\text{S4})$$

8 where $R(\Delta a)$ is the material's crack growth resistance at a crack length Δa .

9 By taking the equality sign in Equation (S4) and evaluating it for $\Delta a \rightarrow 0$, the fracture initiation toughness

10 is given by

$$R(0) = -\frac{1}{2\sqrt{a(D-a)}} \left. \frac{d\Pi(\Delta a; w_s)}{d\Delta a} \right|_{\Delta a=0}, \quad (\text{S5})$$

11 which is identical to Equation (2).

12 S2 The effect of moisture on the bending behavior of *E. aspergillum* spicules

13 We performed our fracture tests in air on sections of *Ea.* spicules obtained from dry *Ea.* skeletons. How-
14 ever, in its native state the *Ea.* sponge lives anchored to the sea floor. It has been shown that the mechani-
15 cal behaviors of some biological materials (such as nacre ,^[?] antler ^[?] and bone ^[?]) change drastically
16 if they are dried out prior to mechanical testing. For example, the work of fracture of nacre that has been
17 soaked in water is almost triple that of nacre that is stored in dry conditions .^[?]

18 To determine whether storing the *Ea.* spicules in dry conditions had a significant effect on their mechani-
19 cal behavior, we soaked sections of 11 *Ea.* spicules in artificial seawater for 16 days and then performed
20 three-point bending tests on them using the procedure described in .^[?]

21 After soaking an *Ea.* spicule section in artificial seawater, we placed it across a trench cut in a cut in a
22 steel plate. The trench span, L , was measured from optical micrographs to be 1.278 mm. We used the
23 same mechanical testing device described in Section 2 and in ^[?] to load the spicule sections in three-
24 point bending and measure F and w_0 until they failed. However, unlike the experiments described in
25 Section 2 we did not notch the spicule sections nor did we glue their ends to the steel plate before testing
26 them. After each test we mounted the pieces of the broken spicule to a aluminum stub, coated them in 10
27 nm of carbon and imaged them in a scanning electron microscope (SEM). We measured each spicule's
28 diameter, D , at the cross-section where it failed from SEM images.

29 We used the slope k_i of the initial linear portion of the spicule's $F-w_0$ response to compute the Young's
30 moduli of both the 11 wet spicules and the 33 dry spicules whose $F-w_0$ responses were previously re-
31 ported in .^[?] We computed the Young's moduli using Euler-Bernoulli beam theory ^[?] as

$$E = \frac{k_i L^3}{48I}, \quad (\text{S6})$$

32 where $I = \pi D^4/64$. A histogram of the Young's moduli of the wet and dry spicules is shown in Figure
33 S1 (A).

34 The bending failure strains, ε_f , of the dry spicules have already been reported in .^[?] We computed the
35 bending failure strain, ε_f , of the wet spicules using the same procedure, which is described in Section 2
36 of .^[?] We selected points along the spicule's longitudinal axis from a micrograph of the spicule taken
37 during the bending test just before the spicule failed. We fit a polynomial to these points and used it to
38 compute the curvature of the spicule's longitudinal axis. Finally, we computed ε_f using the maximum
39 value of the curvature, κ^* , as $\varepsilon_f = D\kappa^*/2$. We compared ε_f for the wet spicules to ε_f for the dry spicules
40 in Figure S1 (B).

41 From these experiments, we do not see any difference in the Young's modulus or bending failure strain
42 between the dry spicules and the spicules that were soaked in seawater. Bias-corrected accelerated (BCa)
43 confidence intervals (CI) using 10,000 bootstrapped samples indicated no reliable difference in the means
44 of the Young's moduli of the wet and dry spicules (upper: 3.0 GPa; lower: -4.5 GPa). Furthermore, a
45 two-sided t -test for independent samples (equal variances not assumed) also indicated no significant
46 difference in their means (degrees of freedom=12, $t=0.05$, $p=0.96$). Similar results were found when
47 comparing the bending failure strains using both BCa CI (upper: 0.0012; lower: -0.0034) and the t-test
48 (degrees of freedom=12, $t=0.97$, $p=0.35$). From these results we conclude that soaking the spicules in
49 water prior to testing them does not appear to affect their Young's modulus and bending failure strain.
50 Based on these results, we speculate that the toughness properties of the spicules also would not change
51 after being soaked in water.

52 **S3 Details of the computational mechanics model used to compute frac- 53 ture initiation toughness**

54 **S3.1 Model geometry**

55 We describe the geometry of the model using the orthonormal set of Cartesian basis vectors $\{\hat{e}_1, \hat{e}_2, \hat{e}_3\}$,
56 shown in Figure S2 (A), and their corresponding Cartesian coordinates $\{x_1, x_2, x_3\}$. The origin of this

57 coordinate system is \mathcal{O} .

58 The *Ea.* spicules have a relatively constant diameter. Therefore, we modeled each of them as a cylinder
59 of length L and cross-sectional diameter D . To reduce computational cost, we modeled one quarter of
60 each specimen for which $x_1 \in [0, L/2]$ and $x_3 \leq 0$ (see Figure S2 (A)). Thus, the domain of the model for
61 an *Ea.* spicule is

$$\mathcal{B} = \left\{ (x_1, x_2, x_3) \in \mathbb{R}^3 : 0 \leq x_1 \leq \frac{L}{2}, x_3 \leq 0, x_2^2 + x_3^2 \leq \frac{D^2}{4} \right\}.$$

62 The *Ta.* spicules, on the other hand, are tapered along their length. It has been shown that their shape
63 is well described by the profile of the Clausen column .^[?] However, in order to facilitate preparing the
64 CAD model for our computational analysis, we modeled the *Ta.* spicules' shapes as ellipsoids, which is
65 a close approximation to the Clausen column's shape. In each experiment, we assumed that the spicule's
66 geometry was symmetric about the cross-section located beneath the wedge. Consequently, we took the
67 diameter that we measured, D , to be the ellipsoid's minor axis. We did not measure the length (major
68 axis), L_s , of each *Ta.* spicule. However, it has been shown that the *Ta.* spicule's aspect ratio $\lambda = L_s/D$
69 is relatively constant with a mean value of 53.6 and a standard deviation of 8.7 ($N=31$) .^[?] Therefore,
70 for all of the *Ta.* spicules that we mechanically tested, we assumed that $\lambda=53.6$. Again, we modeled one
71 quarter of the specimen to reduce computational cost and therefore the domain of the model for a *Ta.*
72 spicule is

$$\mathcal{B} = \left\{ (x_1, x_2, x_3) \in \mathbb{R}^3 : 0 \leq x_1 \leq \frac{L}{2}, x_3 \leq 0, \frac{(x_1 - L/2)^2}{\lambda^2} + x_2^2 + x_3^2 \leq \frac{D^2}{4} \right\}.$$

73 **S3.2 Boundary conditions**

74 We denote the components of the displacement vector, \mathbf{u} , in the $\hat{\mathbf{e}}_i$ basis as u_i , $i \in \{1, 2, 3\}$. We did not
75 include the notch in the geometry of the model explicitly. Rather, we model the effect of a notch of length

76 a and a crack of length Δa by setting $u_1 = 0$ on $\partial\mathcal{B}_1$ (see Figure S2 (B)), where

$$\partial\mathcal{B}_1 = \left\{ (x_1, x_2, x_3) \in \mathcal{B} : x_1 = \frac{L}{2}, x_2 \geq a + \Delta a - \frac{D}{2} \right\}. \quad (\text{S7})$$

77 This leaves the region of \mathcal{B} for which $x_1 = L/2$ and $x_2 < a + \Delta a - D/2$ traction free, as would be the case
 78 for the faces of a notch or crack. We measured the notch length a for each spicule that we mechanically
 79 tested from micrographs taken during the FIB notching procedure (see Section 2). The values of a are
 80 shown in Tables S1 and S2.

The other boundary conditions in our model (see Figure S2 (A), (B)) are

$$u_1 = u_2 = u_3 = 0 \quad \text{on } \partial\mathcal{B}_2, \quad (\text{S8})$$

$$u_3 = 0 \quad \text{on } \partial\mathcal{B}_3, \quad (\text{S9})$$

$$u_2 = -w_{sim} \quad \text{on } \partial\mathcal{B}_4, \quad (\text{S10})$$

where w_{sim} is the applied displacement and

$$\partial\mathcal{B}_2 = \{(x_1, x_2, x_3) \in \mathcal{B} : x_1 = 0\}, \quad (\text{S11})$$

$$\partial\mathcal{B}_3 = \{(x_1, x_2, x_3) \in \mathcal{B} : x_3 = 0\}, \quad (\text{S12})$$

$$\partial\mathcal{B}_4 = \left\{ (x_1, x_2, x_3) \in \mathcal{B} : x_1 = \frac{L}{2}, x_2^2 + x_3^2 = \frac{D^2}{4}, x_2 > 0.9\frac{D}{2} \right\}. \quad (\text{S13})$$

81 S3.3 Constitutive model

82 Before crack growth initiation, the $F-w_0$ response of both the *Ea.* and *Ta.* spicules is linear (see e.g.,
 83 Figure 5 (C), (D)). This suggests that both the *Ea.* and *Ta.* spicules behave in a linear elastic fashion
 84 until the onset of crack growth. The *Ta.* spicules do not appear to possess any internal architecture (see
 85 Figure 6 (B) and 2 (F)). Based on this observation we assume that they are elastically homogeneous and

86 therefore model them as homogeneous linear elastic solids such that

$$\sigma_{ij} = \frac{E}{1+\nu} \left(\epsilon_{ij} + \frac{\nu}{1-2\nu} \delta_{ij} \sum_{k=1}^3 \epsilon_{kk} \right), \quad (\text{S14})$$

87 where σ_{ij} and ϵ_{ij} , $i, j \in \{1, 2, 3\}$ are, respectively, the components of the Cauchy stress tensor, σ , and
88 the infinitesimal strain tensor, ϵ , in the dyadic basis $\hat{e}_i \otimes \hat{e}_j$. The strain components can be computed
89 from the displacements as $\epsilon_{ij} = (\partial u_i / \partial x_j + \partial u_j / \partial x_i) / 2$, $i, j \in \{1, 2, 3\}$. The symbol δ_{ij} is the Kronecker
90 delta, which is equal to unity when $i = j$ and is zero otherwise. The parameters E and ν are the Young's
91 modulus and Poisson's ratio, respectively.

92 While the *Ea.* spicules are clearly not homogeneous, we model them as homogeneous linear elastic solids
93 as well. Because of this modeling assumption, the values of $R(0)$ that we obtain for the *Ea.* spicules
94 should be considered "effective" fracture initiation toughness.

95 For each *Ea.* and *Ta.* spicule that we mechanically tested, we measured D and L from micrographs (see
96 Tables S1 and S2) and computed the compliance of the completely failed specimen $C_f = w_f/F_f$ from
97 the $F-w_0$ data (see Tables S1 and S2). A completely failed spicule can be modeled as two cantilevers
98 that share the load equally. In this completely failed state, the effective Young's modulus can be com-
99 puted using Euler-Bernoulli beam theory as $E = L^3 / 48C_f I$, where $I = \pi D^4 / 64$. We did not measure the
100 Poisson's ratio ν and took its value to be 0.2, which is typical for glass .^[?]

101 **S3.4 Equilibrium equations and solution**

102 In equilibrium, the Cauchy momentum equation requires that

$$\text{Div}(\sigma) = 0 \quad \text{on } \mathcal{B}, \quad (\text{S15})$$

103 where $\text{Div}(\cdot)$ is the divergence operator.

104 We solved Equation (S14) and (S15) subject to the boundary conditions Equation (S7)–(S10) for a given
105 value of Δa using finite element methods .^[?] A representative finite element mesh is shown in Figure S2
106 (C). The mesh consists of constant strain tetrahedron elements. Figure S3 (A), (B) shows contours of the

¹⁰⁷ σ_{11} component of the Cauchy stress obtained from the finite element calculations.

¹⁰⁸ **S3.5 Calculation of fracture initiation toughness using the computational me-** ¹⁰⁹ **chanics model**

¹¹⁰ The experiment described in Section 2 consists of a specimen with a crack placed in series with a linear
¹¹¹ spring (see e.g., Figure 5 (A)). We denote the elastic compliance of this spring as C_m and the elastic com-
¹¹² pliance of the specimen as $C(\Delta a)$, where Δa is the length of the crack. By moving the translation stage,
¹¹³ we apply a displacement w_s to the spring-specimen system. This consequently results in a displacement
¹¹⁴ of the specimen given by

$$w_0(\Delta a; w_s) = \frac{w_s C(\Delta a)}{C_m + C(\Delta a)}. \quad (\text{S16})$$

¹¹⁵ For a fixed w_s , the potential energy of the system is

$$\Pi(\Delta a; w_s) = \frac{w_s^2}{2} \frac{1}{C_m + C(\Delta a)} \quad (\text{S17})$$

¹¹⁶ By substituting Equation (S16) and (S17) into Equation (2), the fracture initiation toughness is given by

$$R(0) = \frac{1}{2} \left(\frac{w_c}{C(0)} \right)^2 \frac{1}{2\sqrt{a(D-a)}} \left. \frac{dC(\Delta a)}{d\Delta a} \right|_{\Delta a=0}, \quad (\text{S18})$$

¹¹⁷ where w_c is the value of w_0 at the initiation of crack growth.

¹¹⁸ In contrast to the experiment described above, our computational mechanics model is displacement con-
¹¹⁹ trolled and therefore the machine compliance $C_m = 0$. We denote the applied displacement in the simu-
¹²⁰ lation as w_{sim} and simplify Equation (S17) to be

$$\Pi_{sim}(\Delta a; w_{sim}) = \frac{w_{sim}^2}{2C(\Delta a)}. \quad (\text{S19})$$

¹²¹ Computing the derivative of Π_{sim} in Equation (S19) gives us

$$\frac{d\Pi_{sim}(\Delta a; w_{sim})}{d\Delta a}\Big|_{\Delta a=0} = -\frac{1}{2} \left(\frac{w_{sim}}{C(0)} \right)^2 \frac{dC(\Delta a)}{d\Delta a}\Big|_{\Delta a=0}. \quad (\text{S20})$$

¹²² Finally, combining Equation (S18) and (S20) we find that

$$R(0) = - \left(\frac{w_c}{w_{sim}} \right)^2 \frac{1}{2\sqrt{a(D-a)}} \frac{d\Pi_{sim}(\Delta a; w_{sim})}{d\Delta a}\Big|_{\Delta a=0}. \quad (\text{S21})$$

¹²³ To compute $R(0)$ using Equation (S21) we must first compute $d\Pi_{sim}/d\Delta a|_{\Delta a=0}$ from the computational
¹²⁴ mechanics model described above.

¹²⁵ For each spicule that we mechanically tested we generated four models with different crack lengths
¹²⁶ $\Delta a = nh$, where $h = 0.08D$ and $n \in \{-2, -1, 1, 2\}$. As we varied the crack length Δa , we kept the applied
¹²⁷ displacement fixed at w_{sim} . For each model we solved for the equilibrium displacement field using finite
¹²⁸ element methods [?] as described in the preceding sections. We computed the potential energy of the
¹²⁹ system as

$$\Pi_{sim}(\Delta a; w_{sim}) = 4 \int_{\mathcal{B}} \frac{E}{2(1+\nu)} \sum_{i=1}^3 \sum_{j=1}^3 \left[\frac{1}{2} \left(\frac{\partial u_i}{\partial x_j} \frac{\partial u_i}{\partial x_j} + \frac{\partial u_i}{\partial x_j} \frac{\partial u_j}{\partial x_i} \right) + \frac{\nu}{1-2\nu} \frac{\partial u_i}{\partial x_i} \frac{\partial u_j}{\partial x_j} \right] d\mathcal{B}. \quad (\text{S22})$$

¹³⁰ The factor of four in front of the integral in Equation (S22) comes from the fact that our computational
¹³¹ mechanics model consists of one quarter of the full specimen. Values of $\Pi_{sim}(\Delta a; w_{sim})$ for a repre-
¹³² sentative spicule are shown in Figure S3 (C). Finally, the derivative $d\Pi_{sim}/d\Delta a$ in Equation (S21) was
¹³³ computed numerically using the central finite difference method such that

$$\frac{d\Pi_{sim}(\Delta a; w_{sim})}{d\Delta a}\Big|_{\Delta a=0} = \frac{\Pi_{sim}(-2h; w_{sim}) - 8\Pi_{sim}(-h; w_{sim}) + 8\Pi_{sim}(h; w_{sim}) - \Pi_{sim}(2h; w_{sim})}{12h} + O(h^4), \quad (\text{S23})$$

¹³⁴ where O is the Landau symbol “big-O.”

¹³⁵ Using this procedure we computed $R(0)$ from Equation (S21) for each spicule that we mechanically
¹³⁶ tested. The values of $R(0)$ are shown in Tables S1 and S2.

137 **S4 Details of the variational fracture method**

138 **S4.1 Variational fracture theory**

139 Motivated by the work of Ambrosio and Tortorelli ,^[?,?] the variational fracture theory (VFT) was put
140 forward by Francfort and Marigo ^[?] to model the evolution of cracks in brittle solids.

141 In it, the solution displacement field, \mathbf{u} , and the crack (or system of cracks), Γ , are postulated to be
142 those that globally minimize the system's total potential energy. However, from what is understood
143 and observed about the physics and mechanics of fracture, it is more reasonable to postulate that the
144 experimentally observed (\mathbf{u}, Γ) are only local minimizers of the total potential energy. There are also
145 several other limitations in VFT about what type of fracture scenarios it can model. Despite the over-
146 constraints on the solution (\mathbf{u}, Γ) in the VFT and its other limitations, it has been shown that its predictions
147 of crack paths are surprisingly close to experimental observations .^[?,?] Considering that, we used the
148 VFT to study the effect of a weak interface's geometry on its ability to enhance the work of fracture (see
149 Section 3).

It is typically quite challenging to solve for (\mathbf{u}, Γ) in the VFT, even using numerical methods. In order to obtain a numerical solution, the VFT is regularized (see Bourdin et. al ^[?] for details) so that the total energy is

$$E_\ell(\mathbf{u}, d) = \int_{\mathcal{B}} (1-d)^2 \Psi_0(\mathbf{x}, \mathbf{u}) d\mathcal{B} + \int_{\mathcal{B}} \frac{G_c}{2} \left(\frac{d(\mathbf{x})^2}{\ell} + \ell \|\nabla d(\mathbf{x})\|^2 \right) d\mathcal{B}, \quad (\text{S24})$$

150 The first term on the right hand side of Equation (S24) is the strain energy stored in the solid, while the
151 second term is the energy of the new surface area created by the growth of the crack. In Equation (S24),
152 Ψ_0 is the strain energy density, \mathbf{x} is the position vector of a material point in the solid \mathcal{B} , and \mathbf{u} is the
153 displacement field. The operator $\|\cdot\|$ is the Euclidean 2-norm, and $\nabla(\cdot)$ is the gradient operator with
154 respect to \mathbf{x} . For a brittle material, the crack growth resistance, R is constant and we take its value to be
155 G_c .

156 The crack is represented by the scalar valued field d , termed the “phase field” or the “damage field”,

157 which takes values between zero and unity. The field d indicates the extent of damage in the material
 158 such that at $d = 1$ the material is fully damaged and at $d = 0$ it is completely intact. Therefore, the crack is
 159 the set of points in \mathcal{B} for which d is close to unity. The parameter ℓ is called the regularization parameter.
 160 It has been shown that the minimizers of the energy given by Equation (S24) converge to the minimizers
 161 of the energy in the VFT theory as $\ell \rightarrow 0$ (see [?, ?, ?] for details).

162 While cracks in RVFT are defined to be subsets of \mathcal{B} and therefore have finite thickness, this does not
 163 preclude RVFT from being a useful and predictive theory of fracture. However, for the cracks in RVFT to
 164 be physically meaningful their thicknesses should be much smaller than the dimensions of the solid. This
 165 is because the crack region has zero stiffness. Consequently, if a cracks thickness is not much smaller
 166 than the solids dimensions then the failure behavior is more similar to plastic failure than brittle fracture.
 167 It is argued that the thickness of the crack is of the order of ℓ . [?] Therefore, by choosing ℓ to be much
 168 smaller than the characteristic dimension of the solid one can ensure that the results have the physical
 169 features of brittle fracture. However, from a practical perspective, the computational cost grows inversely
 170 with ℓ . This leads to what may be the greatest limitation of RVFT—it is computationally expensive. This
 171 limits the complexity of the architectures and size of the specimens that can be modeled. This is part
 172 of the reason that we only model two layers and their adjoining interface for the planar and cylindrical
 173 layered architectures that we discuss in Section 3

174 A necessary condition for \mathbf{u} and d (which is a representation of Γ) to be minimizers of E_ℓ is that they
 175 satisfy Equation (S15), in which $\sigma = (1 - d)^2 \partial \Psi_0 / \partial \epsilon$, and

$$G_c \ell \nabla \cdot (\nabla d) - \frac{G_c d}{\ell} = -2(1 - d)\Psi_0, \quad \text{on } \mathcal{B}. \quad (\text{S25})$$

subject to the boundary conditions

$$\mathbf{u} = \hat{\mathbf{u}}, \quad \text{on } \partial \mathcal{B}_u, \quad (\text{S26a})$$

$$\sigma \mathbf{n} = \mathbf{t}, \quad \text{on } \partial \mathcal{B}_t, \quad (\text{S26b})$$

$$\nabla d \cdot \mathbf{n} = 0, \quad \text{on } \partial \mathcal{B}, \quad (\text{S26c})$$

176 where $\partial\mathcal{B}$ is the boundary of the solid, $\partial\mathcal{B}_u$ is the part of $\partial\mathcal{B}$ on which displacements $\hat{\mathbf{u}}$ are prescribed,
177 and $\partial\mathcal{B}_t$ is the rest of the boundary on which tractions \mathbf{t} are prescribed. The symbol \mathbf{n} is the outward
178 normal vector on $\partial\mathcal{B}$.

179 We solved Equation (S15) and (S25), subject to the boundary conditions given by Equation (S26) using
180 the finite element-based procedure detailed in .^[?] The results from this calculation are shown in Figure 9.

181 S4.2 Regularized variational fracture model for interfaces

182 In this work, we modified the regularized VFT (RVFT) proposed by ^[?] to allow us to model interfaces
183 with different fracture toughnesses within a solid. We did so by spatially varying G_c such that $G_c = G_c(\mathbf{x})$.
184 However, the difference between the dimensionality of an interface (a subset of \mathbb{R}^2) and a solid (a subset
185 of \mathbb{R}^3) results in the same problem that arises when modeling cracks in the VFT. We overcame this
186 problem using a similar regularization strategy as was used in RVFT. Namely, we replaced the interface
187 with a thin interfacial region of thickness $m\ell$, where $m \in \mathbb{R} > 0$ is a fixed constant, so that as $\ell \rightarrow 0$ the
188 interfacial region becomes vanishingly thin. We chose $G_c(\mathbf{x})$ to be a piecewise continuous function so
189 that $G_c = G_I$ in the interfacial region, and $G_c = G_b$ in the bulk material. In the simulations whose results
190 we present in Section 3 we take $m = 2$ and $\ell = 0.05$ mm.

191 To reduce the computational cost of our virtual experiments, we assumed that the crack path was sym-
192 metric about $x_1 = L/2$ and $x_3 = 0$ (see Figure 9). Therefore, we modeled one quarter of the geometry for
193 which $x_1 \in [0, L/2]$ and $x_3 \leq 0$ and imposed the boundary conditions $u_1 = 0$ at $x_1 = L/2$ and $u_3 = 0$ at
194 $x_3 = 0$.

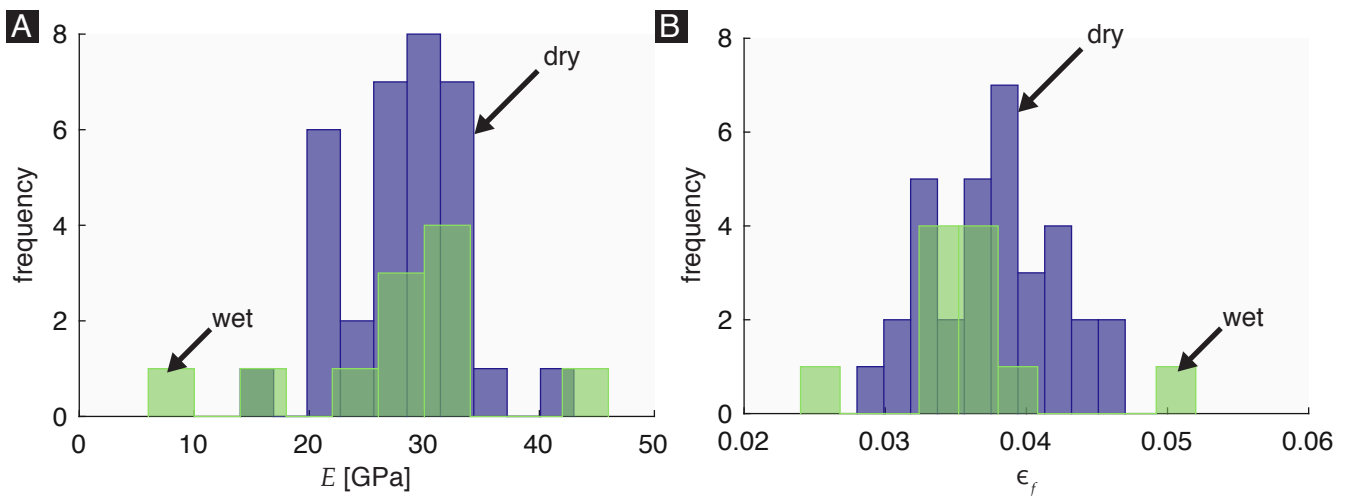


Figure S1. Effect of moisture on the mechanical properties of *Ea.* spicules. (A) A histogram of the effective Young's modulus, E , for 33 dry *Ea.* (light blue) and 11 wet *Ea.* (green) spicules. The mean \pm standard error of E for the dry and wet spicules is 28.1 ± 0.9 GPa and 28.0 ± 2.9 Gpa, respectively. (B) A histogram of the bending failure strain, ϵ_f , for 33 dry *Ea.* (light blue) and 11 wet *Ea.* (green) spicules. The mean \pm standard error of ϵ_f for the dry and wet spicules is 0.0377 ± 0.0008 and 0.0358 ± 0.0019 , respectively.

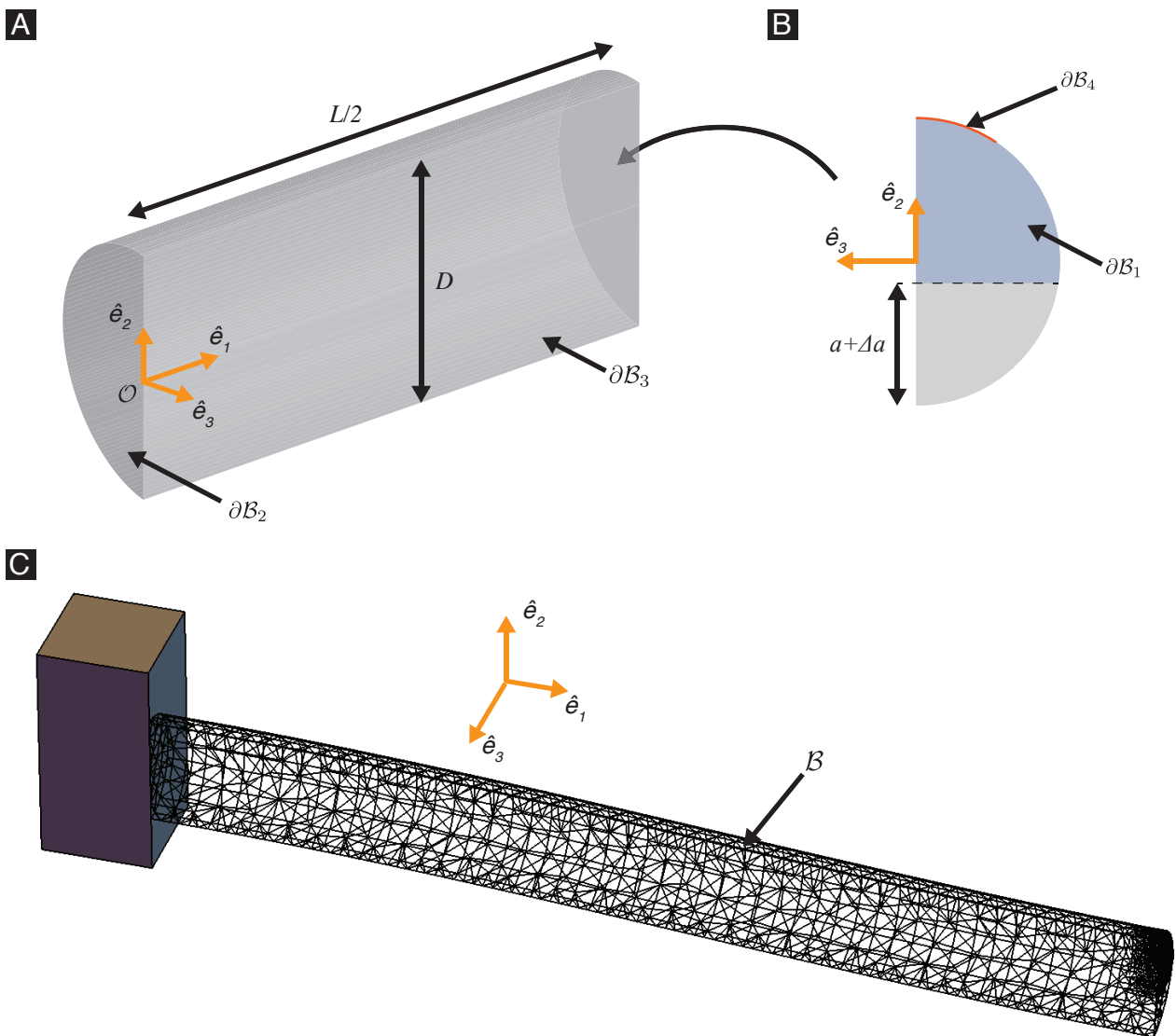


Figure S2. Computational mechanics model of the spicules. (A) Geometry of the *Ea.* model consisting of one quarter of the specimen. The Cartesian basis vectors and origin of the Cartesian coordinate system \mathcal{O} are shown. (B) A view of the model's cross section at $x_1 = L/2$ showing the boundaries $\partial\mathcal{B}_1$ and $\partial\mathcal{B}_4$. (C) The deformed finite element mesh of a representative *Ea.* model.

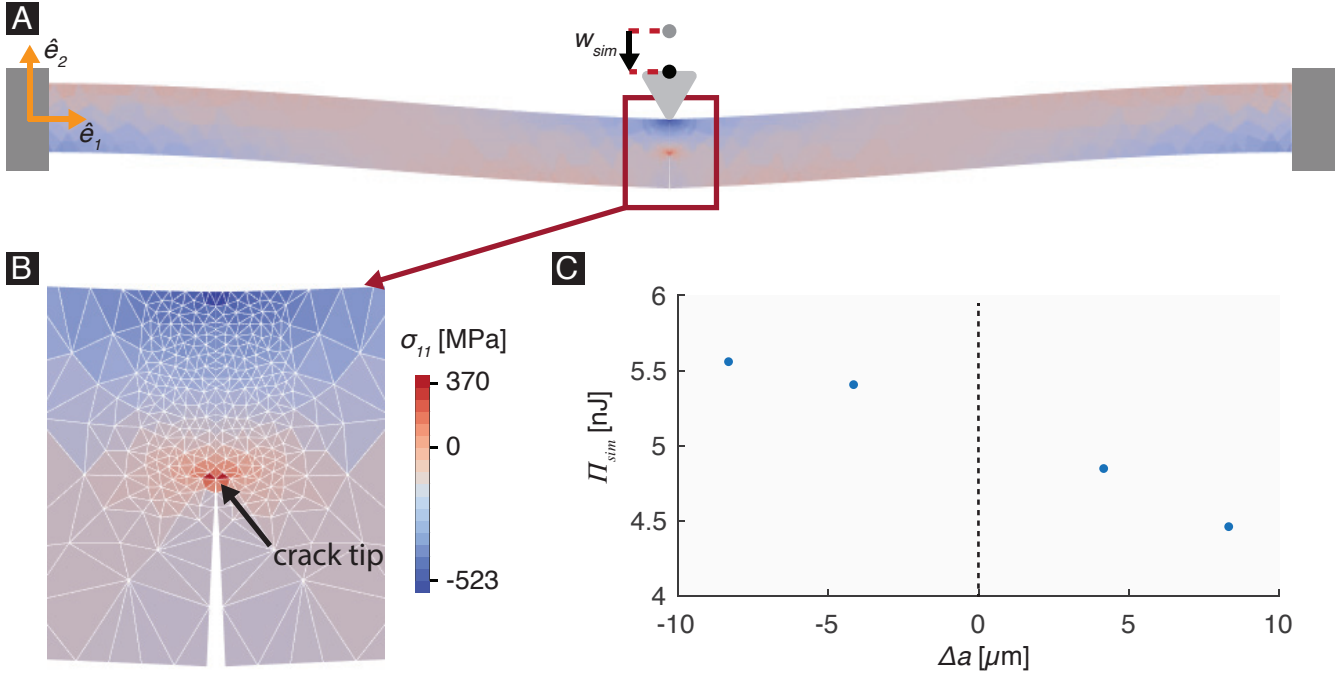


Figure S3. Results of computational mechanics model. (A) Contours of σ_{11} on the surface $\partial\mathcal{B}_3$ (see Figure S2 (A)) shown in the deformed configuration for a representative Ea . model. The displacements are scaled by a factor of 4. (B) A magnified view of the σ_{11} contours near $x_1 = L/2$. The largest tensile stress (red) occurs near the tip of the crack. (C) The values of Π_{sim} for different Δa obtained from the computational mechanics model for a representative Ea . spicule. This data is used to compute the spicule's fracture initiation toughness in Section 2.3. We did not compute the value of Π at $\Delta a = 0$ since it is not required for computing the energy release rate (see Equation (S23)).

Table S1. Ea. spicule data. L is the length; D is the diameter of the cross-section midway along the length; a is the notch length; r_n is the notch root radius; $\alpha = a/D$ is the dimensionless notch length; (w_c, F_c) and (w_f, F_f) are the (w_0, F) points at pop-in and complete failure, respectively; $R(0)$ is the fracture initiation toughness; and $\langle R \rangle$ is the average crack growth resistance.

Specimen ID	Specimen dimensions (see Figure 4)					F and w_0 measurements (see Figure 5)				Toughness (see Figure 7)	
	L [μm]	D [μm]	a [μm]	r_n [nm]	α	w_c [μm]	F_c [mN]	w_f [μm]	F_f [mN]	$R(0)$ [Jm^{-2}]	$\langle R \rangle$ [Jm^{-2}]
Ea1	604.8	50.75	16.13	25	0.32	3.6	13.37	45.7	52.08	7.62	241.96
Ea2	813.0	37.44	10.83	84	0.29	6.9	4.54	42.3	9.40	7.94	75.35
Ea3	814.6	36.57	9.19	251 ^{a)}	0.25	35.8	24.02	40.1	9.04	—	— ^{c)}
Ea4	820.5	23.46	4.31	24	0.18	9.9	1.23	76.1	2.60	2.77	— ^{c)}
Ea5	813.0	25.14	10.13	36	0.40	8.6	1.07	27.7	1.01	6.28	28.28
Ea6	814.6	21.60	13.81	77	0.64	8.8	0.54	28.0	0.72	9.30	23.32
Ea7	820.5	47.07	19.05	300 ^{a)}	0.40	1.7	8.26	38.2	27.95	—	118.68
Ea8	813.0	46.79	14.90	372 ^{a)}	0.32	2.5	11.87	41.0	28.07	—	169.99
Ea9	808.8	46.50	14.92	120	0.32	2.3	7.60	47.6	28.91	1.66	101.20
Ea10	808.8	27.74	7.60	229 ^{a)}	0.27	28.3	9.81	39.9	3.44	—	— ^{c)}
Ea11	813.0	32.81	15.82	39	0.48	3.7	1.41	28.6	3.53	2.61	25.59
Ea12	820.5	31.33	17.09	69	0.55	— ^{b)}	—	33.0	2.86	—	63.25
Ea13	783.3	22.94	7.22	39	0.31	4.7	0.81	21.7	0.88	1.62	— ^{c)}
Ea14	814.6	45.65	22.29	45	0.49	5.9	6.51	49.1	17.73	10.76	136.12
Ea15	814.6	45.51	21.62	84	0.47	— ^{b)}	—	38.8	15.89	—	118.86
Ea16	808.8	45.59	21.34	79	0.47	— ^{b)}	—	34.6	14.80	—	— ^{c)}
Ea17	775.2	51.97	14.86	90	0.29	2.1	4.89	72.8	54.02	1.44	141.87
Ea18	783.3	57.76	18.15	178	0.31	2.1	7.33	52.5	53.60	1.86	170.28
Ea19	790.5	62.61	18.55	84	0.30	2.3	12.01	63.2	76.14	1.94	238.54
Ea20	820.5	64.40	23.36	89	0.36	1.9	14.19	97.6	153.63	1.91	383.81
Ea21	814.6	70.42	24.44	44	0.35	2.6	20.28	68.5	139.05	3.76	335.33
Ea22	779.6	43.16	17.26	52	0.40	1.7	2.54	30.7	15.16	1.11	— ^{c)}
Ea23	813.0	50.83	19.82	118	0.39	2.6	7.58	82.9	49.56	2.15	278.43
Ea24	814.6	53.12	14.98	57	0.28	2.9	8.95	67.0	48.87	2.59	132.91
Ea25	775.2	57.24	32.40	112	0.57	— ^{b)}	—	46.8	55.94	—	258.58
Ea26	814.6	24.56	3.07	137	0.13	— ^{b)}	—	103.0	2.19	—	— ^{c)}
Ea27	813.0	44.17	2.97	37	0.07	42.5	59.37	121.9	13.99	33.85	— ^{c)}
Ea28	820.5	24.06	2.96	186	0.12	17.9	2.66	22.0	0.81	7.49	— ^{c)}
Ea29	820.5	33.13	3.94	43	0.12	— ^{b)}	—	86.4	10.69	—	— ^{c)}
Ea30	775.2	40.21	6.24	51	0.16	— ^{b)}	—	54.0	18.54	—	— ^{c)}
Ea31	783.3	35.42	6.68	193	0.19	4.1	4.48	62.2	14.09	2.03	— ^{c)}
Ea32	820.5	39.29	3.06	159	0.08	46.3	77.24	83.6	4.76	27.20	— ^{c)}
Ea33	814.6	29.51	3.64	136	0.12	— ^{b)}	—	69.3	4.56	—	— ^{c)}
Ea34	775.2	46.92	4.41	153	0.09	25.7	78.30	94.1	12.64	19.46	— ^{c)}
Ea35	783.3	34.02	5.07	136	0.15	— ^{b)}	—	84.8	12.43	—	— ^{c)}

^{a)} Red text indicates values of r_n that exceed the threshold for valid measurement of $R(0)$ as per Section 2.3;

^{b)} Values of w_c and F_c could not be obtained for this specimen since we could not reliably identify the pop-in event.

^{c)} In this specimen, the value of ΔF_c exceeded 15% of the value of F_c and therefore we did not consider crack growth to be predominantly stable.

Table S2. *Ta*. spicule data. L is the length; D is the diameter of the cross-section midway along the length; a is the notch length; r_n is the notch root radius; $\alpha = a/D$ is the dimensionless notch length; (w_c, F_c) and (w_f, F_f) are the (w_0, F) points at pop-in and complete failure, respectively; $R(0)$ is the fracture initiation toughness; and $\langle R \rangle$ is the average crack growth resistance.

Specimen ID	Specimen dimensions (see Figure 4)					F and w_0 measurements (see Figure 5)				Toughness (see Figure 7)	
	L [μm]	D [μm]	a [μm]	r_n [nm]	α	w_c [μm]	F_c [mN]	w_f [μm]	F_f [mN]	$R(0)$ [Jm^{-2}]	$\langle R \rangle$ [Jm^{-2}]
Ta1	775.2	23.67	5.72	107	0.24	4.4	0.93	13.7	0.43	0.81	— ^{c)}
Ta2	783.3	28.00	13.06	365 ^{a)}	0.47	8.9	1.60	25.1	2.09	—	— ^{c)}
Ta3	790.5	30.34	12.71	129	0.42	6.6	0.60	27.1	0.66	1.66	— ^{c)}
Ta4	601.3	43.61	11.17	63	0.26	3.1	8.66	41.2	23.64	3.93	130.89
Ta5	601.3	36.17	15.92	50	0.44	4.7	4.26	34.0	10.03	10.46	— ^{c)}
Ta6	597.2	34.69	8.29	35	0.24	3.1	3.46	40.6	12.77	3.16	— ^{c)}
Ta7	604.8	24.05	8.69	79	0.36	2.6	0.86	20.3	1.88	1.46	19.55
Ta8	601.3	27.84	10.82	87	0.39	4.1	1.49	15.8	2.25	5.47	— ^{c)}
Ta9	603.8	31.13	10.67	28	0.34	2.1	1.70	24.1	5.89	1.62	— ^{c)}
Ta10	597.2	37.37	9.37	82	0.25	3.2	5.10	31.0	11.79	3.70	69.94
Ta11	604.8	37.56	14.23	127	0.38	2.9	3.83	34.5	14.94	4.82	84.65
Ta12	597.2	34.45	7.85	216 ^{a)}	0.23	3.9	3.94	27.1	10.92	—	29.91
Ta13	820.5	42.62	3.59	151	0.08	8.6	7.64	66.1	0.49	0.12	— ^{c)}
Ta14	779.6	26.10	3.57	161	0.14	10.4	2.72	61.4	1.84	1.68	— ^{c)}
Ta15	775.2	41.42	3.32	190	0.08	7.4	9.18	40.5	11.20	4.02	— ^{c)}
Ta16	790.5	29.81	3.03	121	0.10	9.6	4.07	25.4	2.10	3.68	— ^{c)}
Ta17	820.5	34.65	3.56	207 ^{a)}	0.10	— ^{b)}	—	25.5	1.68	—	— ^{c)}
Ta18	814.6	31.63	4.31	193	0.14	8.2	4.20	33.1	3.84	3.29	— ^{c)}
Ta19	779.6	38.34	3.14	174	0.08	8.4	9.18	36.7	8.44	4.27	70.40
Ta20	813.0	28.42	3.20	198	0.11	15.6	4.77	22.8	1.32	6.15	— ^{c)}
Ta21	779.6	28.27	2.66	234 ^{a)}	0.09	16.1	7.84	25.5	2.43	—	— ^{c)}
Ta22	775.2	31.46	3.49	148	0.11	7.9	6.16	46.2	7.42	4.60	— ^{c)}
Ta23	783.3	29.86	4.13	151	0.14	9.0	6.09	20.8	2.80	5.28	— ^{c)}
Ta24	808.8	27.90	5.02	180	0.18	9.0	4.03	17.8	1.39	4.07	— ^{c)}
Ta25	783.3	29.97	4.25	217 ^{a)}	0.14	9.3	6.23	16.5	1.73	—	— ^{c)}
Ta26	790.5	29.87	5.21	181	0.17	9.3	5.43	19.0	1.90	4.75	— ^{c)}

^{a)} Red text indicates values of r_n that exceed the threshold for valid measurement of $R(0)$ as per Section 2.3;

^{b)} Values of w_c and F_c could not be obtained for this specimen since we could not reliably identify the pop-in event.

^{c)} In this specimen, the value of ΔF_c exceeded 15% of the value of F_c and therefore we did not consider crack growth to be predominantly stable.